Decoding and encoding of visual patterns using magnetoencephalographic data represented in manifolds

CrossMark

Po-Chih Kuo [a], Yong-Sheng Chen [a,b,*], Li-Fen Chen [c,d,**], Jen-Chuen Hsieh [c,d]

[a] Department of Computer Science, National Chiao Tung University, Hsinchu, Taiwan
[b] Institute of Biomedical Engineering, National Chiao Tung University, Hsinchu, Taiwan
[c] Institute of Brain Science, National Yang-Ming University, Taipei, Taiwan
[d] Integrated Brain Research Unit, Department of Medical Research, Taipei Veterans General Hospital, Taipei, Taiwan

ARTICLE INFO

ABSTRACT

Visual decoding and encoding are crucial aspects in investigating the representation of visual information in the human brain. This paper proposes a bidirectional model for decoding and encoding of visual stimulus based on manifold representation of the temporal and spatial information extracted from magnetoencephalographic data. In the proposed decoding process, principal component analysis is applied to extract temporal principal components (TPCs) from the visual cortical activity estimated by a beamforming method. The spatial distribution of each TPC is in a high-dimensional space and can be mapped to the corresponding spatiotemporal component (STC) on a low-dimensional manifold. Once the linear mapping between the STC and the wavelet coefficients of the stimulus image is determined, the decoding process can synthesize an image resembling the stimulus image. The encoding process is performed by reversing the mapping or transformation in the decoding model and can predict the spatiotemporal brain activity from a stimulus image. In our experiments using visual stimuli containing eleven combinations of checkerboard patches, the information of spatial layout in the stimulus image was revealed in the embedded manifold. The correlation between the reconstructed and original images was 0.71 and the correlation map between the predicted and original brain activity was highly correlated to the map between the original brain activity for different stimuli ($r = 0.89$). These results suggest that the temporal component is important in visual processing and manifolds can well represent the information related to visual perception.

© 2014 Published by Elsevier Inc.

Introduction

Decoding brain activity evoked in the visual cortices and encoding visual stimuli are challenging yet worthwhile endeavors. Modeling the visual processes in the brain can help to establish the connection between visual stimuli and brain activity. This connection can be described using decoding and encoding models (Kriegeskorte, 2011; Naselaris et al., 2011). Once the model parameters are obtained via a training procedure, a decoding model can be used to recognize events from specific patterns of brain activity or even reconstruct the contents of the stimuli. In contrast, an encoding model can be used to predict brain responses corresponding to perceived environmental events. Numerous studies have investigated decoding and encoding models by conducting experiments using sensory stimuli (Brouwer and Heeger, 2009; Cox and Savoy, 2003; Formisano et al., 2008; Haxby et al., 2001; Haynes and

Rees, 2005; Kamitani and Tong, 2005; Kay et al., 2008; Mitchell et al., 2008; Miyawaki et al., 2008; Naselaris et al., 2009; Nishimoto et al., 2011; Ramkumar et al., 2013; Schoenmakers et al., 2013; Thirion et al., 2006), mental imagery (Reddy et al., 2010), and movement (Bradberry et al., 2010; Gallivan et al., 2011). By correlating the data/feature space of neural responses and that of the stimuli, decoding and encoding models can be constructed for the classification of perceptual data or the reconstruction of the stimuli (Fujiwara et al., 2013; Naselaris et al., 2011). Classification is achieved by identifying the most likely stimulus according to brain response patterns whereas reconstruction is an attempt to reproduce the perceived stimuli.

In studies on functional magnetic resonance imaging (fMRI), conventional classifier was used as a simple decoding method to differentiate the brain response patterns represented in a discriminative feature space (Brouwer and Heeger, 2009; Cox and Savoy, 2003; De Martino et al., 2008; Haynes and Rees, 2006; Kamitani and Tong, 2005; LaConte et al., 2007; Norman et al., 2006; Reddy et al., 2010). This kind of method is data-driven and is restricted to the classification of a fixed set of categories. Another approach is to identify novel stimuli by predicting its corresponding brain responses, usually achieved by a general encoding model. Kay et al. (2008) proposed a method to identify

* Correspondence to: Department of Computer Science, National Chiao Tung University, 1001 University Road, Hsinchu, Taiwan. Fax: +886 3 5721490.
** Correspondence to: Institute of Brain Science, National Yang-Ming University, No. 155, Sec. 2, Linong Street, Taipei, Taiwan. Fax: +886 2 28273123.
E-mail addresses: kuopc@cs.nctu.edu.tw (P.-C. Kuo), yschen@cs.nctu.edu.tw (Y.-S. Chen), lfchen@ym.edu.tw (L.-F. Chen), jchsieh@ym.edu.tw (J.-C. Hsieh).

novel natural images according to the brain activity predicted by a receptive-field model. Mitchell et al. (2008) constructed a computational model to map semantic features to brain responses in order to predict brain activity and identify new words viewed by subjects. Furthermore, visual stimuli can be reconstructed using blood oxygenation level-dependent (BOLD) signals in the visual cortex. Multi-voxel decoders and multi-scale image representation have been used to reconstruct visual symbols and characters (Miyawaki et al., 2008). Combining models with different Bayesian priors can help to rebuild natural images (Naselaris et al., 2009). Recently, visual experiences of natural movies have been reconstructed by a stimulus–response encoding model (Nishimoto et al., 2011).

Retinotopic mapping has been measured and defined from visual input to the neurons in the primary visual cortex by fMRI-based experimentation (Brewer et al., 2005; Engel et al., 1997; Sereno et al., 1995; Wandell et al., 2007). Because of the relationship between visual stimulus and the invoked neural activity, the decoding of visual processing depends largely on the spatial distribution of neuronal activation in the visual cortex. When modeling this relationship, therefore, multivariate analysis of functional neuroimaging data can be adopted to ensure a comprehensive consideration of the information related to all voxels in the visual cortex. Multi-voxel pattern analysis (MVPA) was demonstrated to be capable of distinguishing among activity patterns revealed by multiple voxels and estimating the contribution of voxels to specific stimuli (De Martino et al., 2008; Haynes and Rees, 2006; Liang et al., 2013; Norman et al., 2006; Parkes et al., 2009). Voxels with high discriminative ability were regarded as important features spanning the subspace of task-related brain responses and were obtained by a supervised learning process in MVPA.

Manifold learning is an unsupervised learning method and can be used to find an embedded non-linear manifold on which the data lie in the original higher-dimensional space. Manifold can well organize the data in a lower-dimensional space by preserving the neighborhood relationship between proximal data points in the original space. Intrinsic structure of data organization unveiled by a manifold can be further analyzed or visualized for exploring its underlying characteristics. Previous studies applied manifold-based learning methods to the image data and obtained manifolds revealing the organization of image data in various aspects, for example, object poses, facial expressions, or lighting directions (Roweis and Saul, 2000; Tenenbaum et al., 2000). In neuroscience field, applying manifold learning method to functional neuroimaging data is an emerging research direction. Seung and Lee (2000) suggested that patterns of neural activity form a manifold while observing faces with various orientations or scales. Because the dimensionality of perceptual inputs is enormous, they speculated that the brain might use an efficient way to represent the complex input of neuronal signals from sensory receptors. Adoption of a model similar to the representation in the brain may facilitate the recognition of novel stimuli (Kriegeskorte, 2011). Ogmen and Herzog (2010) recently investigated the limitations of retinotopic mapping and suggested that local manifold representations should be considered. Furthermore, studies suggested that such high-dimensional neural data can be concisely represented using a low-dimensional nonlinear manifold (Miikkulainen et al., 2005; Ritter et al., 1992; Roweis and Saul, 2000; Tenenbaum et al., 2000). When represented by a manifold, its subspace might convey perceptual meanings or higher-level concepts of neural activity.

Taking advantage of high temporal resolution, electroencephalography (EEG) and magnetoencephalography (MEG) have been used to reconstruct rapidly changing stimuli or movements. From the acquired MEG signals, natural speech can be identified using classical canonical correlation analysis (Koskinen et al., 2013). Three-dimensional hand movements were also reconstructed using EEG signals (Bradberry et al., 2010). In the studies of visual decoding, MEG responses evoked by visual stimuli of different orientation columns were identified using multivariate classifiers (Duncan et al., 2010). Rapid visual

information processing of low-level visual features can be decoded from MEG signals (Ramkumar et al., 2013). Multivariate analysis method was applied on source-space MEG data for the decoding of different image categories (van de Nieuwenhuijzen et al., 2013). Although spatial patterns are known to be an essential element in visual processing, the spatiotemporal components (STCs) are also very important (Ahlfors et al., 1999; Ayzenshtat et al., 2010; Ioannides et al., 2012; van de Nieuwenhuijzen et al., 2013) and might be beneficial for the decoding of visual processing.

This paper proposes a bidirectional decoding/encoding model that can be used to reconstruct visual patterns containing eleven different combinations of checkerboard patches from spatiotemporal brain activity. This model can also be used to predict the brain activity for a given visual stimulus. The proposed model uses two-dimensional wavelets for the representation of image stimuli and manifold for the representation of the brain activity in the visual cortex. These two representations are both reversible and hence we can establish forward and inverse connections between brain activity and image stimulus by calculating two-way mappings between the two representations. Based on the previous hypothesis regarding the manifold representation of sensory neurons, this study investigated whether manifold representation can benefit the reconstruction of visual patterns. We also utilized the temporal information of brain activity and derived the STCs for both decoding and encoding processes. Unlike the previous studies which used fMRI for visual reconstruction, we examined the possibility of reconstructing elementary visual patterns from temporal brain activity measured by MEG.

Materials and methods

Subjects and recordings

Seven subjects (five males and two females, aged 22–26) with normal or corrected-to-normal vision participated in this study. During data acquisition, the subjects sat in a comfortable chair in front of a screen which was 1 m away from their eyes and were instructed to look at the center of the visual stimulus passively while keeping their heads steady. Each subject participated in five sessions, each of which consisted of 220 trials. As shown in Fig. 1(a), each trial began with a fixation cross displayed on the screen for a random duration between 650 ms and 850 ms. Following fixation, an image was randomly selected from the set of visual stimuli containing eleven different combinations of checkerboard patches. Four stimulus images containing only one patch were categorized as the basic image set, and the rest of the stimulus images as the composite image set, as shown in Fig. 1(b). The field of view of each image was $26° × 26°$ and that of each checkerboard patch was $6.5° × 6.5°$. The eccentricity was $10.5°$ from the center of the checkerboard patch to the center of the screen. Each stimulus image was statically displayed on the screen for 250 ms, as shown in Fig. 1(a). A 5-min break was given between each session to prevent the subjects from fatigue.

MEG data were recorded in a magnetically shielded room using a 306-channel whole-head system (Vectorview system, Neuromag Ltd., Finland) at a sampling rate of 1001.6 Hz and were filtered with passband 0.03 to 330 Hz. Among the set of channels, MEG data from 204 gradiometers were used for further processing. Vertical and horizontal electrooculograms (EOGs) were also recorded to detect eye blinking. Three-dimensional T1-weighted magnetic resonance imaging (MRI) with the MP-RAGE sequence was performed using a Siemens scanner with TR = 2530 ms, TE = 3.03 ms, TI = 1100 ms, FOV = $224 × 256 × 192$ mm^3, matrix size = $224 × 256 × 192$, and voxel size = $1 × 1 × 1$ mm^3. Coordinate systems between the MRI volume and MEG device were co-registered by locating three landmarks (nasion, left and right pre-auricular points) in both systems. This study was approved by the Institutional Review Board of

(a)

(b)
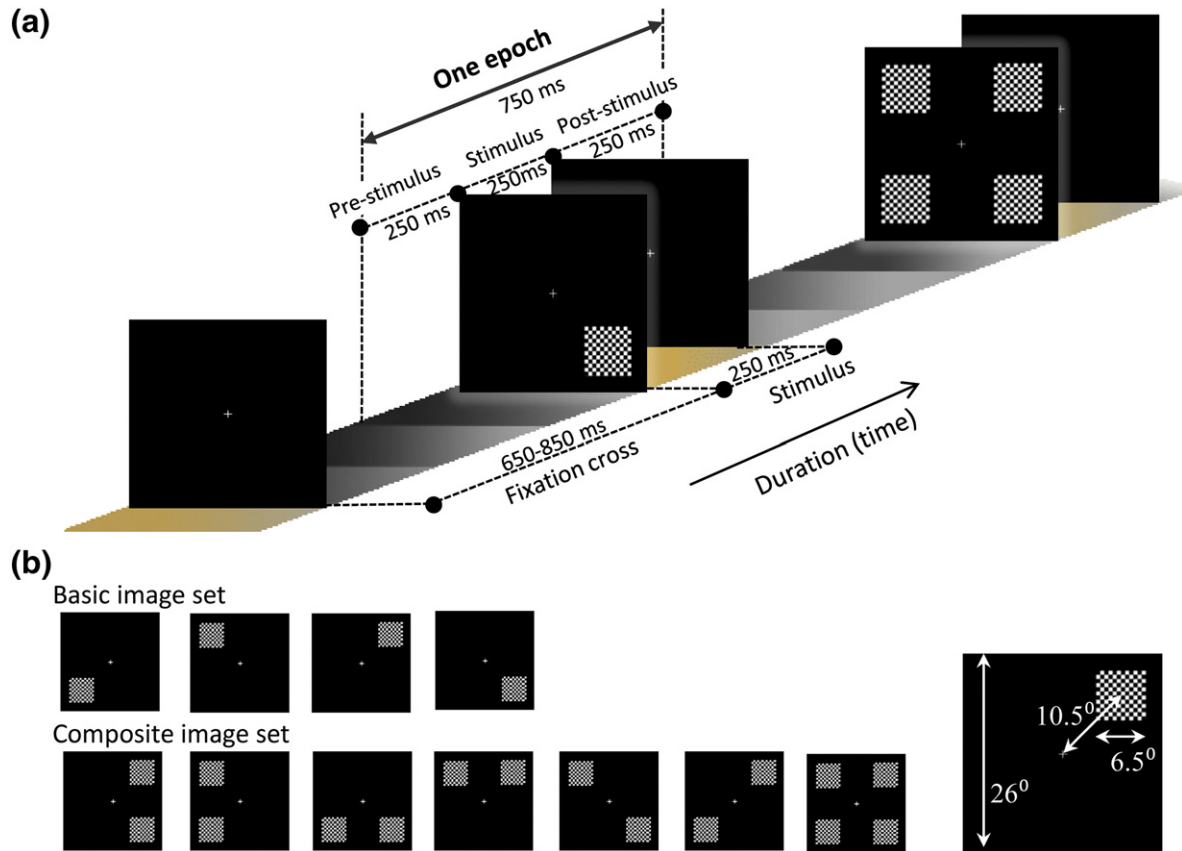
Fig. 1. (a) Timeline in an epoch of MEG experiment in this study. A stimulus randomly selected from eleven images was displayed for 250 ms after a fixation cross with random time interval between 650 ms and 850 ms. One epoch included a 250-ms pre-stimulus fixation cross, a 250-ms static stimulus image, and a 250-ms post-stimulus fixation cross. (b) There were eleven combinations of checkerboard patches in the stimulus images, including four images in the basic image set and seven images in the composite image set. The fields of view of stimulus image and checkerboard patch were 26° × 26° and 6.5° × 6.5°, respectively. The eccentricity was 10.5° from the center of the checkerboard patch to the center of the screen.

Taipei Veterans General Hospital and written informed consents were obtained from all subjects.

Data preprocessing

Trials were excluded from our analysis if they contained gradiometer signals with amplitudes exceeding 2000 fT/cm or EOG signals with amplitudes greater than 250 μV. MEG signals were projected onto a signal subspace by the signal space projection method (Uusitalo and Ilmoniemi, 1997) and passed through a band-pass filter (2–50 Hz). For baseline correction, the mean amplitude of the pre-stimulus interval [−250 ms, −50 ms] was subtracted from the signal of each trial. EOG-free epochs of 750 ms starting from 250 ms prior to the stimulus onset were extracted for further analysis.
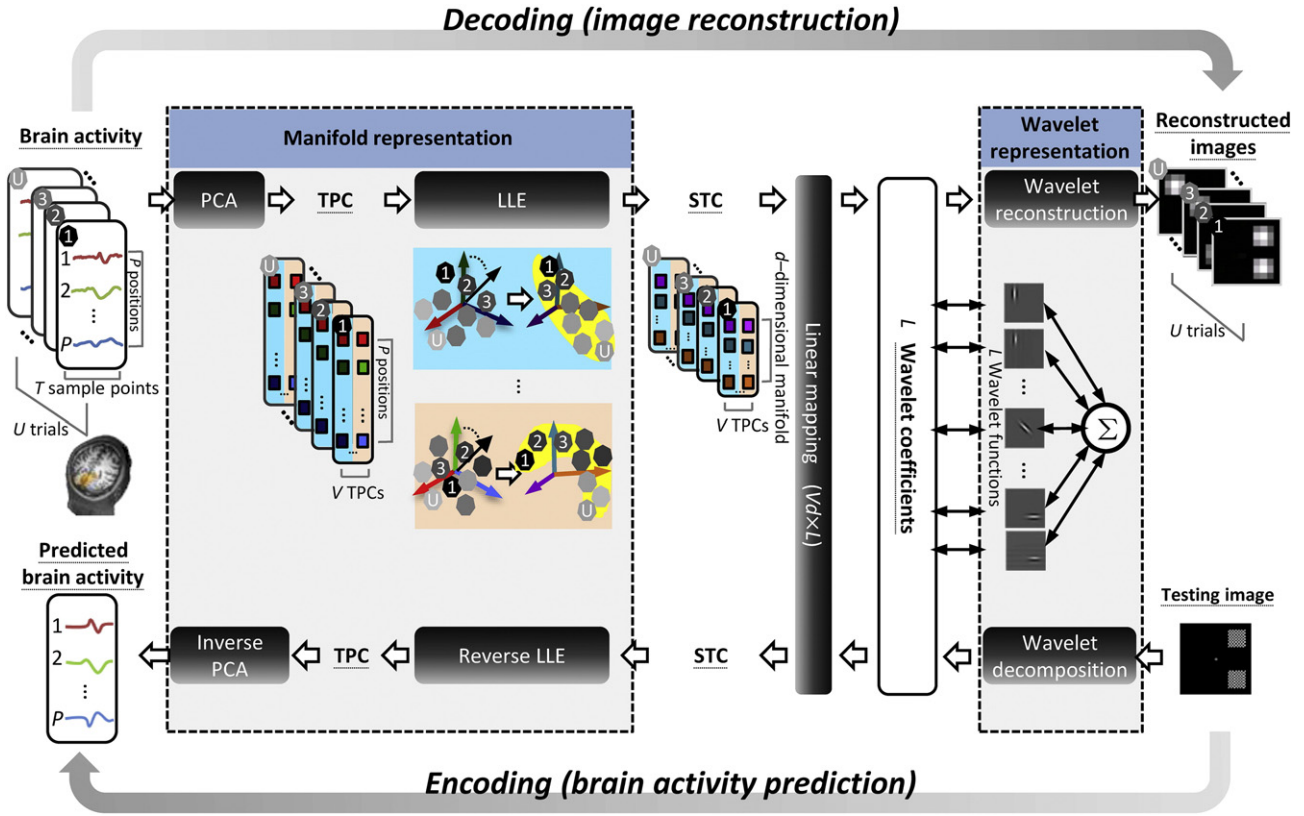
Bidirectional model for decoding and encoding

Fig. 2 presents the proposed bidirectional model for decoding and encoding. The cortical activity for the position located at the center of each MRI voxel within the primary visual cortex (V1) was estimated from the MEG signals using the source estimation method described in the following section. In the proposed manifold representation of cortical activity, we first applied principal component analysis (PCA) to extract temporal principal components (TPCs) from all trials of cortical activity in V1. To reduce the spatial dimensionality of the TPCs, we applied the locally linear embedding (LLE) method (Roweis and Saul, 2000) to map the TPC data to its corresponding STC in a lower-

dimensional space, while preserving the neighborhood relationship between the TPC data in the original space. The STCs form a manifold as essential features representing the cortical activity. Through linear mapping, the STCs were used to calculate the wavelet coefficients for the reconstruction of stimulus images represented by a wavelet basis. In contrast with the above-mentioned decoding process, the encoding process can be engaged to predict brain activity for a given visual stimulus, as shown in Fig. 2. For a given image, we first calculated its wavelet coefficients and converted them into STC. Reverse LLE was applied to map the STC to its corresponding TPCs. Finally, inverse PCA was applied to back-project the TPCs to the predicted brain activity of each position. The details of the proposed model are described in the following sections.

Estimation of cortical activation

This study applied the maximum contrast beamformer (MCB) method (Chen et al., 2006) to estimate brain activity in V1 from the measurements $b(t)$ recorded by MEG sensors, where $t = 1, ..., T$ and T is the total number of sample points. The segmentation of V1 was achieved by registering the MRI of each subject to the template containing Brodmann area labels provided by MRIcro (Chris Rorden, University of Nottingham, UK). The number of voxels in V1 ranged from 20,035 to 26,378 for the seven subjects. For each targeted position p at the center of each MRI voxel in V1, l was defined as the lead field vector containing the predicted measurements of N MEG sensors for a unit dipole. For the given S different kinds of stimuli and P positions, MCB was used to calculate a spatial filter

Fig. 2. The proposed bidirectional model for decoding and encoding. The model contains manifold and wavelet representation for brain activity and stimulus image, respectively. In the decoding process, TPCs are calculated by applying PCA to the time course of brain activity. LLE is then applied to the spatial distribution of each TPC to obtain STC lying on a manifold. Following linear mapping, STC is transformed into wavelet coefficients, which are used to reconstruct the stimulus image through the weighted summation of wavelet functions. In the encoding process, a test stimulus image is decomposed into wavelet coefficients according to the wavelet representation. The coefficients are then transformed into STCs using the inverse of linear mapping. Then reverse LLE is applied to the STC to obtain TPCs and the brain activity is predicted by applying inverse PCA to the TPCs.

$\hat{\boldsymbol{w}}_{p,s}$ for stimulus s, $s = 1, ..., S$, and position p, $p = 1, ..., P$, by minimizing the variance of the output signal $x_{p,s}(t) = \boldsymbol{w}_{p,s}^{\mathrm{T}}\boldsymbol{b}(t)$ under the unit-gain constraint $\boldsymbol{w}_{p,s}^{\mathrm{T}}\boldsymbol{l} = 1$:

$$\hat{\boldsymbol{w}}_{p,s} = \arg\min_{\boldsymbol{w}_{p,s}} \left[\mathrm{E}\left\{ \left(x_{p,s}(t) - \mathrm{E}\left\{ x_{p,s}(t) \right\} \right)^2 \right\} + \alpha \left\| \boldsymbol{w}_{p,s} \right\|^2 \right]$$
$$\text{subject to } \boldsymbol{w}_{p,s}^{\mathrm{T}}\boldsymbol{l} = 1, \tag{1}$$

where $\mathrm{E}\{\cdot\}$ denotes the expectation value and α is the parameter of Tikhonov regularization for restricting the norm of the spatial filter $\boldsymbol{w}_{p,s}$. The use of Lagrange multipliers enabled us to solve this constrained optimization problem in order to obtain the analytical solution of $\hat{\boldsymbol{w}}_{p,s}$:

$$\hat{\boldsymbol{w}}_{p,s} = \arg\min_{\boldsymbol{w}_{p,s}} \left[\boldsymbol{w}_{p,s}^{\mathrm{T}}(\boldsymbol{C} + \alpha\boldsymbol{I})\boldsymbol{w}_{p,s} \right] \text{ subject to } \boldsymbol{w}_{p,s}^{\mathrm{T}}\boldsymbol{l} = 1$$
$$= \frac{(\boldsymbol{C} + \alpha\boldsymbol{I})^{-1}\boldsymbol{l}}{\boldsymbol{l}^{\mathrm{T}}(\boldsymbol{C} + \alpha\boldsymbol{I})^{-1}\boldsymbol{l}}, \tag{2}$$

where $\boldsymbol{C} = \mathrm{E}\{(\boldsymbol{b}(t) - \mathrm{E}\{\boldsymbol{b}(t)\})^2\}$ is the $N \times N$ covariance matrix of MEG measurements $\boldsymbol{b}(t)$ for stimulus s and $\boldsymbol{I}$ is the $N \times N$ identity matrix. We then averaged the S spatial filters, $\hat{\boldsymbol{w}}_{p,s}$, $s = 1, ..., S$, of all stimuli to obtain the spatial filter $\overline{\boldsymbol{w}}_p$ at position p:

$$\overline{\boldsymbol{w}}_p = \frac{1}{S}\sum_{s=1}^{S}\hat{\boldsymbol{w}}_{p,s}. \tag{3}$$

After passing MEG measurements of i-th trial $\boldsymbol{b}^i(t)$, $i = 1, ..., U$, through the spatial filter $\overline{\boldsymbol{w}}_p$, we calculated the brain activity $x_p^i(t)$ of the i-th trial at position p:

$$x_p^i(t) = \overline{\boldsymbol{w}}_p^{\mathrm{T}}\boldsymbol{b}^i(t). \tag{4}$$

Here U is the total number of MEG trials comprising the data for all stimuli.

Temporal PCA

To represent the temporal information of brain activity in a more condensed manner, temporal PCA was applied to the estimated brain activity across all stimuli, trials, and positions. The resulting principal components $\boldsymbol{Z}$ are given by the following:

$$\boldsymbol{Z} = \boldsymbol{A}^{\mathrm{T}}\boldsymbol{X}, \tag{5}$$

where the $((p-1) \times U + i)$-th column of $\boldsymbol{X}_{T \times PU}$ contains the T mean centered sample points of brain activity data $x_p^i(t)$, $t = 1, ..., T$, for the i-th trial ($i = 1, ..., U$) at the p-th position ($p = 1, ..., P$), as defined below:

$$\boldsymbol{X} = \begin{bmatrix} x_1^1(1) - \overline{x}(1) & \cdots & x_1^U(1) - \overline{x}(1) & \cdots & x_P^1(1) - \overline{x}(1) & \cdots & x_P^U(1) - \overline{x}(1) \\ x_1^1(2) - \overline{x}(2) & \cdots & x_1^U(2) - \overline{x}(2) & \cdots & x_P^1(2) - \overline{x}(2) & \cdots & x_P^U(2) - \overline{x}(2) \\ \vdots & & \vdots & & \vdots & & \vdots \\ x_1^1(T) - \overline{x}(T) & \cdots & x_1^U(T) - \overline{x}(T) & \cdots & x_P^1(T) - \overline{x}(T) & \cdots & x_P^U(T) - \overline{x}(T) \end{bmatrix},$$
$$\overline{x}(t) = \frac{1}{PU}\sum_{p=1}^{P}\sum_{i=1}^{U}x_p^i(t). \tag{6}$$

Each column of the obtained matrix $\mathbf{Z}_{V \times PU}$ contains V TPCs in the form $z_p^i(v)$, $v = 1, \ldots, V$:

$$\mathbf{Z} = \begin{bmatrix} z_1^1(1) & \cdots & z_1^U(1) & \cdots & z_P^1(1) & \cdots & z_P^U(1) \\ z_1^1(2) & \cdots & z_1^U(2) & \cdots & z_P^1(2) & \cdots & z_P^U(2) \\ & \vdots & & \vdots & & \vdots & \\ z_1^1(V) & \cdots & z_1^U(V) & \cdots & z_P^1(V) & \cdots & z_P^U(V) \end{bmatrix}. \tag{7}$$

Matrix $\mathbf{A}$ is a transformation matrix, the columns of which contain V eigenvectors corresponding to the V largest eigenvalues of the unbiased covariance matrix $\mathbf{\Sigma} = \frac{1}{PU-1}\mathbf{X}^{\mathrm{T}}\mathbf{X}$.

Using transformation matrix $\mathbf{A}$ enabled us to reduce temporal dimensionality from T to V and transform the original data into corresponding TPCs lying on the linear space spanned by $\mathbf{A}$. Data related to brain activity under examination $\mathbf{x}_p^\theta = [x_p^\theta(1), x_p^\theta(2), \ldots, x_p^\theta(T)]^{\mathrm{T}}$ at position p was also transformed using matrix $\mathbf{A}$ into its corresponding TPC $\mathbf{z}_p^\theta = [z_p^\theta(1), z_p^\theta(2), \ldots, z_p^\theta(V)]^{\mathrm{T}}$:

$$\mathbf{z}_p^\theta = \mathbf{A}^{\mathrm{T}}\left(\mathbf{x}_p^\theta - \overline{\mathbf{x}}\right), \tag{8}$$

where $\overline{\mathbf{x}} = [\overline{\mathbf{x}}(1), \overline{\mathbf{x}}(2), \ldots, \overline{\mathbf{x}}(T)]^{\mathrm{T}}$.

LLE with correlation as distance metrics

For each position p in V1, we calculated its TPCs using the method described in the previous section. For each TPC, the LLE method (Roweis and Saul, 2000) was used to determine the manifold embedded in the spatial distribution of brain activation. LLE is an unsupervised method capable of reducing dimensionality according to the similarity between data in the original space, without the prior knowledge of stimulus type. For the v-th TPC, the values for all P positions in V1 form a spatial distribution and also can be considered as point $\mathbf{z}^i = [z_1^i(v), z_2^i(v), \ldots, z_P^i(v)]^{\mathrm{T}}$, $i = 1, \ldots, U$, in a P-dimensional space. Let Λ denote the set of all TPCs: $\Lambda = \{\mathbf{z}^1, \cdots, \mathbf{z}^U\}$. For each of these U points in Λ in the P-dimensional space, $\mathbf{z}^i$, the goal of LLE was to transform it to a low-dimensional (d-dimensional) vector $\mathbf{q}^i = [q_1^i(v), q_2^i(v), \ldots, q_d^i(v)]^{\mathrm{T}}$, $i = 1, \ldots, U$:

$$\mathbf{z}^i \in \mathrm{R}^P \rightarrow \mathbf{q}^i \in \mathrm{R}^d, \text{ where } d \ll P. \tag{9}$$

The LLE algorithm first finds the K-nearest neighbors for point $\mathbf{z}^i$, denoted as $\mathbf{z}^{ij} \in \Lambda - \{\mathbf{z}^i\}$, $j = 1, \ldots, K$. The algorithm then represents $\mathbf{z}^i$ as a linear combination of these neighbors, $\sum_{j=1}^{K} B_{ij}\mathbf{z}^{ij}$, where B_{ij}, $j = 1, \ldots, K$, are the weightings determined through the minimization of the error function:

$$\varepsilon_1(B) = \sum_{i=1}^{U} \left\| \mathbf{z}^i - \sum_{j=1}^{K} B_{ij}\mathbf{z}^{ij} \right\|^2. \tag{10}$$

Instead of the Euclidean distance in the original LLE method (Roweis and Saul, 2000), this study adopted the spatial correlation coefficient as the distance measure for finding neighbors in the P-dimensional space of TPC spatial distribution. For point $\mathbf{z}^i$, its K-nearest neighbors, $\mathbf{z}^{ij}$, $j = 1, \ldots, K$, were identified as those having the K-highest correlation coefficients with $\mathbf{z}^i$. Weightings B_{ij} were solved in a least-squares manner as in (Roweis and Saul, 2000). Once the weightings B_{ij}, $j = 1, \ldots, K$, for all data points $\mathbf{z}^i$, $i = 1, \ldots, U$, were obtained, the corresponding data points $\mathbf{q}^i$, $i = 1, \ldots, U$, in the d-dimensional embedded space were calculated through the minimization of the cost function:

$$\varepsilon_2(\Delta) = \sum_{i=1}^{U} \left\| \mathbf{q}^i - \sum_{j=1}^{K} B_{ij}\mathbf{q}^{ij} \right\|^2, \tag{11}$$

where $\Delta = \{\mathbf{q}^1, \cdots, \mathbf{q}^U\}$ and $\mathbf{q}^{ij} \in \Delta$ is the data point in the d-dimensional space corresponding to $\mathbf{z}^{ij}$. By combining the low-dimensional vectors

for all of the V TPCs, vector $\boldsymbol{\gamma}^i$ with $V \times d$ dimensions was constructed as the STC for the i-th trial:

$$\boldsymbol{\gamma}^i = \left[q_1^i(1), q_2^i(1), \ldots, q_d^i(1), q_1^i(2), q_2^i(2), \ldots, q_d^i(2), \ldots, q_1^i(V), q_2^i(V), \ldots, q_d^i(V)\right]^{\mathrm{T}}. \tag{12}$$

In the classification or reconstruction process, the spatial distribution of the v-th TPC under examination, $\mathbf{z}^\theta = [z_1^\theta(v), z_2^\theta(v), \ldots, z_P^\theta(v)]^{\mathrm{T}}$, was linearly represented by its K-nearest neighbors $\mathbf{z}^{\theta j} \in \Lambda$, $j = 1, \ldots, K$, using weightings $B_{\theta j}$, $j = 1, \ldots, K$, determined through the minimization of function $\varepsilon_3(B_\theta) = \|\mathbf{z}^\theta - \sum_{j=1}^{K} B_{\theta j}\mathbf{z}^{\theta j}\|^2$. With the same coefficients in the linear combination of $\mathbf{z}^\theta$, we obtained a low-dimensional representation $\mathbf{q}^\theta = [q_1^\theta(v), q_2^\theta(v), \ldots, q_d^\theta(v)]^{\mathrm{T}} = \sum_{j=1}^{K} B_{\theta j}\mathbf{q}^{\theta j}$, where $\mathbf{q}^{\theta j} \in \Delta$ is the point in the d-dimensional embedded space corresponding to $\mathbf{z}^{\theta j}$ in the original P-dimensional space.

Stimulus image reconstruction

Wavelet representation was used to reconstruct the grayscale stimulus image observed by the subject, as shown in the right part of Fig. 2. First, the estimated wavelet coefficients $\phi_1', \phi_2', \ldots, \phi_L'$ were calculated by the inner product of the STC $\boldsymbol{\gamma}$ and the L weighting vectors $\mathbf{m}_l$, $l = 1, \ldots, L$:

$$\boldsymbol{\phi}' = \begin{bmatrix} \phi_1' \\ \phi_2' \\ \vdots \\ \phi_L' \end{bmatrix} = \mathbf{M}^{\mathrm{T}}\boldsymbol{\gamma}, \tag{13}$$

where $\mathbf{M} = [\mathbf{m}_1 \quad \mathbf{m}_2 \quad \cdots \quad \mathbf{m}_L]$. Next, we calculated the reconstructed image $I(x, y)$ by superimposing the L wavelet functions $\psi_l(x, y)$ weighted by the estimated coefficients ϕ_l', $l = 1, \ldots, L$:

$$I(x, y) = \sum_{l=1}^{L} \phi_l' \psi_l(x, y). \tag{14}$$

Finally, thresholding was applied on pixels to zero negative intensity values caused by the small fluctuation in wavelet functions.

In this work, we used single-trial MEG data to calculate STC for reconstructing images of size 80×80. Four-level 2D Haar wavelet transformation was applied to stimulus images. For comparison, Gabor wavelets were also used because they are well suited to modeling the receptive field in visual cortices (Jones and Palmer, 1987). Because an image can be completely represented by a set of wavelets only when they form a frame (Lee, 1996), this study used Gabor wavelets with eight orientations, two phases, and three scales for the reconstruction of the stimulus images. As in Lee (1996), the mother wavelet of the 2D Gabor is defined as:

$$\psi(x, y) = \frac{1}{\sqrt{2\pi}} e^{-\frac{1}{8}(4x^2 + y^2)} \cdot \left[e^{ikx} - e^{-\frac{k^2}{2}} \right], \tag{15}$$

where $k = 2.5$. Then the 2D admissible wavelet family is given by:

$$\psi_{\alpha,\beta,\mu,w}(x, y) = a_0^{-\alpha}\psi_\theta\left(a_0^{-\alpha}x - \beta b_0, \ a_0^{-\alpha}y - \mu b_0 a_0^\alpha\right), \tag{16}$$

$$\psi_\theta(x, y) = \psi\left(x\cos\left(\frac{\pi}{8}w\right) + y\sin\left(\frac{\pi}{8}w\right), -x\sin\left(\frac{\pi}{8}w\right) + y\cos\left(\frac{\pi}{8}w\right)\right), \tag{17}$$

where $a_0 = 2.0$, $\alpha = 0, 1, 2$ is the dilation in scale, $b_0 = 1.0$ is the unit spatial interval, $w = 1, \ldots, 8$ is the step size of each rotation, $\beta = -20, \ldots, 20$, and $\mu = -20, \ldots, 20$.

The weighting matrix $\mathbf{M}_{Vd \times L}$ for transforming STC into wavelet coefficients was obtained by minimizing the cost function $\varepsilon_4(\mathbf{M})$ with the minimum norm criterion in a least-squares regression. Function $\varepsilon_4(\mathbf{M})$ is defined by the residual between wavelet

coefficients ϕ of the presented image and the estimated wavelet coefficients $\phi' = M^{\mathrm{T}}\gamma$:

$$\varepsilon_4(M) = \|\phi' - \phi\|^2, \quad \text{where } \phi = \begin{bmatrix} \phi_1 \\ \phi_2 \\ \vdots \\ \phi_L \end{bmatrix} = \begin{bmatrix} \langle I(x,y), \psi_1(x,y) \rangle \\ \langle I(x,y), \psi_2(x,y) \rangle \\ \vdots \\ \langle I(x,y), \psi_L(x,y) \rangle \end{bmatrix}. \quad (18)$$

For image reconstruction, the MEG signals evoked by four basic images were converted into STCs and employed in the training process described above to obtain the weighting matrix $M_{Vd \times L}$ in the wavelet-based reconstruction. Tenfold cross validation was used to assess the performance of image reconstruction. In the training procedure of image reconstruction, we randomly selected nine-tenths of the MEG trials evoked by basic image set as the training data and used these data to estimate all parameters in our model. Then the rest of the MEG trials evoked by basic image set and the trials evoked by composite image set constituted the testing data for image reconstruction. For performance evaluation, this study evaluated the similarity between the presented images and the reconstructed ones by calculating the averaged spatial correlation coefficients between images.

Encoding process

The encoding process in the proposed bidirectional model can be used to predict brain activity when a subject observes an image. As shown in Fig. 2, the processing units in the encoding process are the same as those in the decoding process, except with reverse flow. Using the wavelet representation, wavelet decomposition was applied to calculate the wavelet coefficients ϕ of a given stimulus image. As in the training process for the estimation of M, transformation matrix M' was also calculated using the least-squares method with the minimum norm criterion and then was used to map the wavelet coefficients of images onto STC:

$$\gamma' = M'^{\mathrm{T}}\phi. \quad (19)$$

Once the STC were obtained in manifold representation, the following reverse LLE procedure was applied to map STC in low-dimensional manifold space to TPCs in the original high-dimensional space. This reverse mapping was performed by applying the locally linear combination estimated in the manifold space to the data in the original space. First, each segment of STC γ' was represented by a point $q' = [q'_1(v), q'_2(v), \dots, q'_d(v)]^{\mathrm{T}}$, $v = 1, \dots, V$, in d-dimensional space corresponding to the v-th TPC. The weightings B^j_j, j = 1,...,K, for linearly approximating q' from its K-nearest neighbors q^j, j = 1,...,K, were calculated by minimizing the following error function:

$$\varepsilon_5(B) = \left\| q' - \sum_{j=1}^{K} B'_j q^j \right\|^2, \quad (20)$$

where $q^j \in \Delta$ belongs to the training set. Once obtained, the same set of weightings B^j_j was applied in computing the v-th TPC $z' = [z'_1(v), z'_2(v), \dots, z'_P(v)]^{\mathrm{T}}$ in the original P-dimensional space:

$$z' = \sum_{j=1}^{K} B'_j z^j, \quad (21)$$

where $z^j \in \Lambda$, j = 1,...,K, is a training data in P-dimensional space corresponding to q^j in d-dimensional space. Finally, inverse PCA was used to calculate the predicted brain activity X' from all of the V obtained TPCs:

$$X' = A \begin{bmatrix} z'_1(1) & \cdots & z'_P(1) \\ \vdots & \ddots & \vdots \\ z'_1(V) & \cdots & z'_P(V) \end{bmatrix}, \quad (22)$$

where X' can be regarded as a single-trial spatiotemporal brain activity in V1.

We applied tenfold cross validation to evaluate the performance of encoding model. Nine-tenths of the MEG signals for eleven stimuli were used for model parameter estimation. Each of the eleven stimulus images was used to calculate activity profile by using the trained encoding model and the obtained activity was compared with the brain activity estimated by MCB from the remaining one-tenth of the acquired MEG signals.

Classification

The overall performance of the proposed decoding/encoding model was evaluated according to the reconstructed images and predicted brain activity patterns. Furthermore, we performed classification analysis to evaluate the discriminative capability of STC alone, excluding the influences of image representation using wavelets and interconnection between STC and wavelets. The STCs obtained in the decoding process were used by a classifier to assess their discriminative property in differentiating brain activity of different visual stimuli. Moreover, the STCs calculated for all of the brain regions and time intervals were evaluated through classification to determine a set of STCs with high classification accuracy to be used in the decoding process. We also evaluated various combinations of the model parameters V, d, and K within the ranges $V \in [1, 10]$, $d \in [1, 20]$, and $K \in [2, 20]$, and determined the parameter values to achieve high classification accuracy. We found that the classification performance did not change drastically when $V \geq 2$, $d \geq 8$, and $K \geq 12$. The lower bound of V was chosen to ensure that the cumulative contribution rate of eigenvalues was larger than 60%.

Before STC calculation, in classification, MEG data with the same number of trials for each kind of stimulus were first averaged across four trials for noise reduction. Support vector machine (Chang and Lin, 2011) with a linear kernel was used as the classifier and γ with two temporal components and eight manifold dimensions ($V = 2$ and $d = 8$) was used as the input data. The size of neighborhood, K, was set to be 14 in the LLE algorithm. The classification performance of four or eleven kinds of stimuli was evaluated using tenfold cross validation. In each evaluation step, recorded MEG signals evoked by each kind of stimulus images were divided into training and testing data sets before applying temporal PCA and LLE. Only the training data were used to determine the transformation matrix A and the sets of Λ and Δ for TPC/STC calculation. Total accuracy was calculated by averaging accuracy values across tenfolds.

We also compared the classification accuracy obtained by applying LLE to the spatial domain with that obtained by applying PCA. In this case, the dimensionality of spatial principal component was also set to be eight, which was the same as the manifold dimension using LLE. The original TPC data of all positions in V1 without applying spatial processing were also included in the comparison. Moreover, when comparing the results obtained by applying PCA on temporal domain with those without applying temporal PCA, the signal powers were calculated by using brain activity estimated from the 2–50 Hz MEG signals in the period between 60 ms and 160 ms after the stimulus onset.

Manifold representation

It is essential to investigate whether manifold can provide a compact representation of brain activity manifesting high-level properties in the embedded low-dimensional space. In this work, we examined how the spatial layout information of checkerboard patches was revealed in the embedded manifold constructed from the brain activity data evoked by both basic and composite sets. For each subject, eight-dimensional manifold ($d = 8$) with neighborhood size of fourteen ($K = 14$) was calculated by LLE method from the averaged data for every four trials of brain activity evoked by eleven types of stimuli. Moreover, we also assessed the spatial linearity of the STCs to investigate whether the STC of a composite stimulus can be well predicted by linearly combining the STCs of its constituent basic stimuli. To be specific, we examined

how well the combination of basic stimuli was related to the combination of the corresponding brain responses. For each composite stimulus, its predicted STC was first calculated by averaging the STCs of its constituent basic stimuli. The dissimilarity values between the predicted STC and the STCs of the seven composite stimuli were then calculated by Euclidean distance. The image dissimilarity values between the average of the constituent basic stimuli and the seven composite stimuli were also calculated by Euclidean distance. The correlation between STC dissimilarity and stimulus dissimilarity values was calculated and averaged across the seven composite stimuli. This averaged correlation was defined as the spatial linearity index of the STCs. For comparison, we also calculated the spatial linearity index of brain activity using the
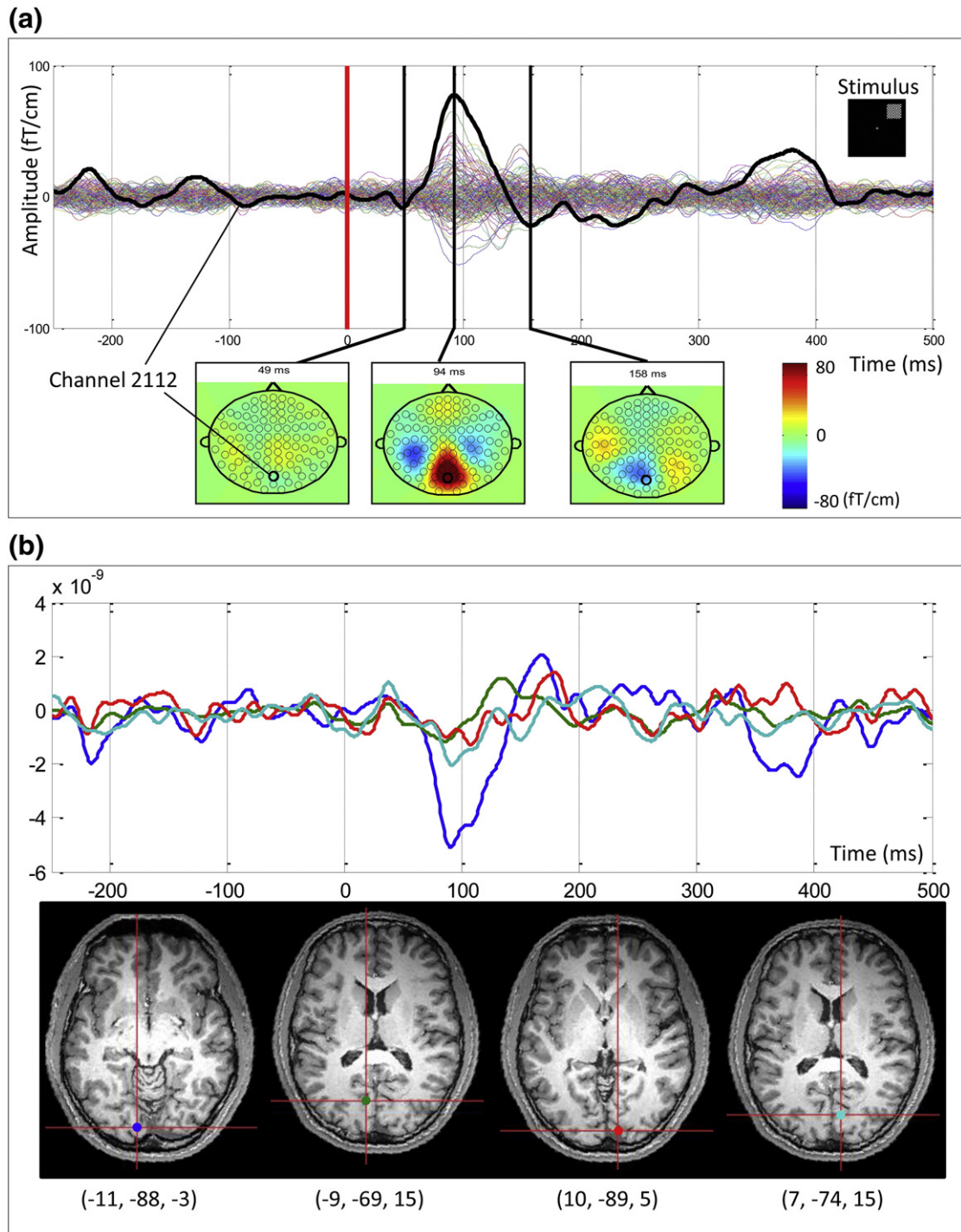
Fig. 3. MEG signals and estimated cortical activity. (a) Time courses of 204-channel MEG signals aligned to the onset of the stimulus (red line) and averaged across trials. The visual stimulus image is presented in the top-right corner. The bold profile illustrates the averaged signals of Channel 2112 with its position shown by the circle on the topographic field map. The topographic field maps depict the spatial distributions of magnetic fields at time points 49 ms, 94 ms, and 158 ms. (b) Brain activity estimated by MCB. Examples of estimated brain activity are illustrated in blue, green, red, and cyan profiles for locations $(-11, -88, -3)$, $(-9, -69, 15)$, $(10, -89, 5)$, and $(7, -74, -15)$, respectively, shown on the MRI in MNI (Montreal Neurological Institute) coordinate system.

above procedure, in which the STC of each stimulus was replaced with its spatiotemporal activity in V1 estimated from the 2–50 Hz MEG signals in the time interval from 60 ms to 160 ms after the stimulus onset.

Results

### MEG sensor signals and estimated cortical activity

Fig. 3(a) illustrates the MEG signals acquired from Subject S1 when presented with the stimulus image shown in the upper right corner. The bold line in the figure indicates a signal at channel 2112 in the occipital area. All trials were aligned to the stimulus onset (0 ms) and then averaged. The first peak of the visual evoked magnetic field (VEF) was found at 94 ms after the stimulus onset. Fig. 3(a) also shows the topographic fields at 49 ms, 94 ms, and 158 ms, in which the position of channel 2112 is indicated by a black circle. Fig. 3(b) presents the temporal profiles and locations of four estimated sources of cortical activity plotted in standardized MNI (Montreal Neurological Institute) space for Subject S1, which are depicted in blue, green, red, and cyan.
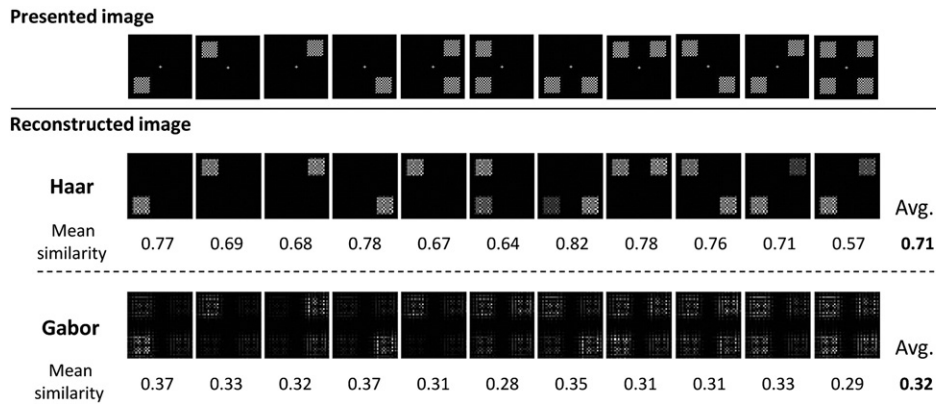
Reconstruction of stimulus image

As shown in Fig. 4(a), the proposed method reconstructed a visual stimulus image containing checkerboard patches from a single trial of
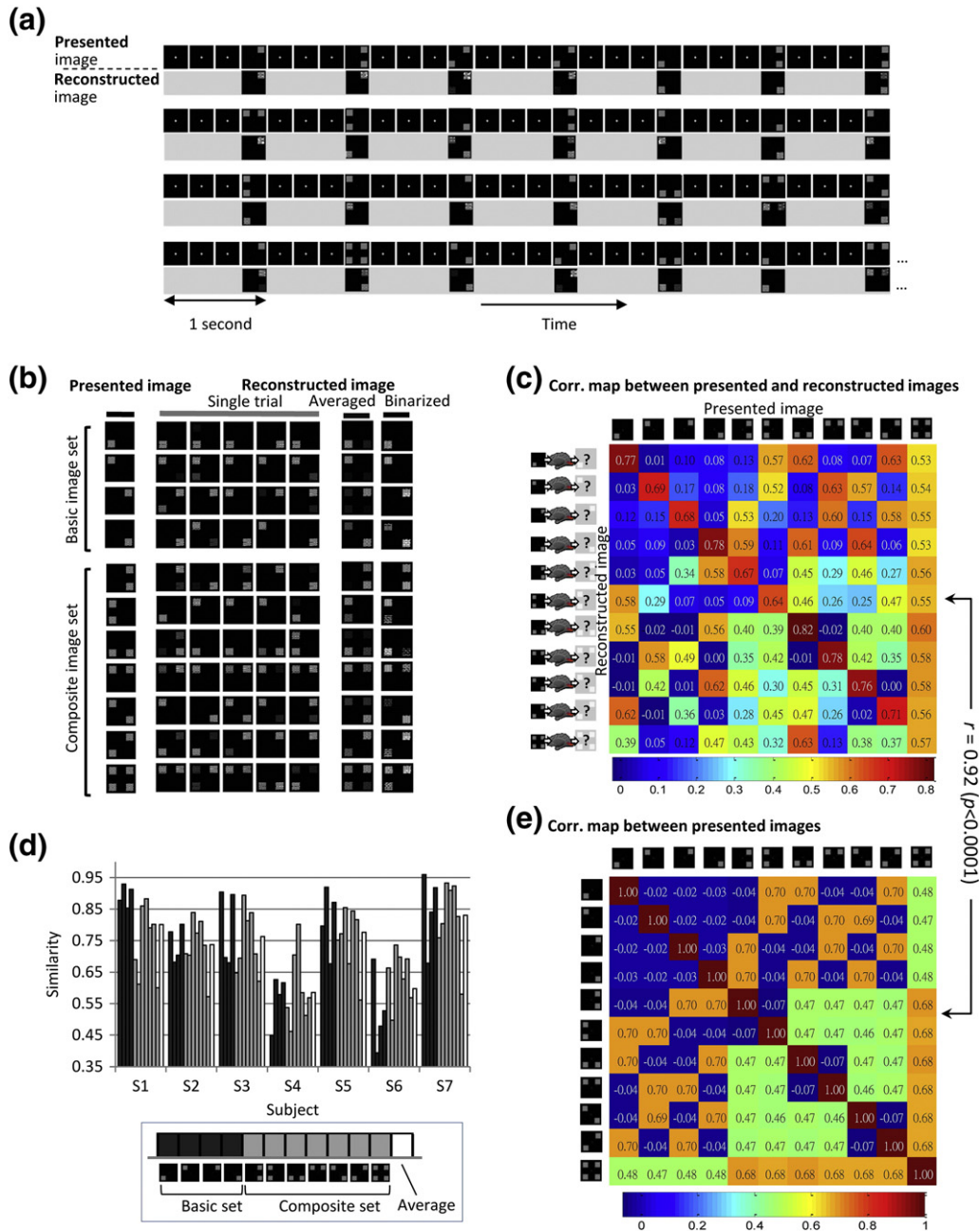
Fig. 4. Results of stimulus image reconstruction. (a) Presented and reconstructed images of each single trial data for Subject S1. Each stimulus image was presented for 250 ms and MEG data from 60 ms to 160 ms after the stimulus onset were used to reconstruct the image. (b) Reconstructed stimulus images after averaging and binarization. Presented are the single trial results of eleven stimulus images. The averaged image was obtained from five reconstructed images and the results after binarization are presented in the rightmost column. (c) Correlation map showing the similarity between the presented and reconstructed images. Similarity value was calculated as the spatial correlation coefficient of presented and reconstructed images for each subject followed by averaging across seven subjects. (d) Similarity between the presented and reconstructed images for each subject. Similarity values for the basic and composite image sets are indicated by black and gray bars, respectively, and the white bars present mean similarity values across all stimulus images. (e) Correlation coefficient map between the presented stimulus images. The correlation coefficient between the correlation maps shown in (c) and (e) was 0.92 (p < 0.0001).

Presented image

Reconstructed image

Haar

| Mean similarity | 0.77 | 0.69 | 0.68 | 0.78 | 0.67 | 0.64 | 0.82 | 0.78 | 0.76 | 0.71 | 0.57 | **Avg.** **0.71** |

Gabor

| Mean similarity | 0.37 | 0.33 | 0.32 | 0.37 | 0.31 | 0.28 | 0.35 | 0.31 | 0.31 | 0.33 | 0.29 | **Avg.** **0.32** |

Fig. 5. Results of stimulus image reconstruction using Haar and Gabor wavelets. Reconstructed images were the single-trial results for Subject S1. The mean similarity values were averaged across all trials and all subjects.

100-ms MEG data. Fig. 4(b) presents the image averaged from the reconstruction results of five trials of MEG data acquired for Subject S1. Averaged and then binarized images are also presented in the two rightmost columns. Fig. 4(c) shows the averaged similarity values calculated by spatial correlation coefficients between the presented images and the reconstructed ones for seven subjects. Fig. 4(d) outlines the similarity for each kind of stimulus from either basic or composite image sets. The averaged similarity among the composite image set was also high, despite the fact that the model was trained using the basic image set. As shown by the white bars in Fig. 4(d), this study calculated the mean similarity averaged across eleven stimulus images for each of the seven subjects. The overall reconstruction result shows considerable promise according to the high mean similarity ($r = 0.59$–0.83). Fig. 4(e) presents the correlation map in which each value is the correlation coefficient between each pair of stimulus images. In addition to values on diagonal, there are high correlation values in some of non-diagonal elements because of the high similarity between stimulus images. The correlation coefficient between the two maps in Figs. 4(c) and 4(e) was 0.92 ($p < 0.0001$). Fig. 5 illustrates the presented images and those reconstructed from one single-trial MEG data of Subject S1 using either Haar or Gabor wavelets. The mean values of similarity between the presented and reconstructed images were averaged across all trials and all subjects.

Encoding of stimulus image

Fig. 6(a) illustrates the spatial distribution of the original and predicted brain activity for Subject S1, at seven time points ranging from 90 ms to 150 ms following the stimulus onset. Here the original brain activity means the cortical activity estimated by MCB from MEG measurements. The first row depicts the predicted brain activity for the stimulus image shown in the leftmost column, as calculated in the encoding process of the proposed bidirectional model. The following eleven rows depict the original brain activity for all of the eleven stimuli presented in the leftmost column. The rightmost column shows the spatiotemporal correlation values between the predicted activity and the original ones. The activity evoked by the same stimulus presented the highest correlation value ($r = 0.82$, $p < 0.001$).

Fig. 6(b) presents three correlation maps for predicted/original activity, original brain activity, and stimulus images. Each value in the predicted/original brain activity correlation map was the average of the correlation coefficients between the predicted and the original brain activity across all trials and all subjects. The diagonal values in this map ranged from 0.19 to 0.58, demonstrating a positive correlation between the predicted and original activity. In the original brain activity correlation map, each element shows the averaged correlation coefficient value of original brain activity across all trials and all subjects. Moreover, the correlation coefficients between these three correlation

maps are also shown in Fig. 6(b). First, the correlation value was significantly positive ($r = 0.84$, $p < 0.0001$) between the correlation maps of stimulus images and original brain activity. Second, the correlation map of original brain activity was also significantly correlated to the correlation map between predicted and original activity ($r = 0.89$, $p < 0.0001$). Last, there was a highly positive correlation between the predicted/original brain activity correlation map and stimulus image correlation map ($r = 0.74$, $p < 0.0001$). Fig. 6(c) shows the similarity between original and predicted spatiotemporal activity with respect to the same stimuli. For each subject, the similarity values are indicated by black and gray bars for basic and composite image sets, respectively, and the white bars indicate mean similarity values across all kinds of stimulus images.
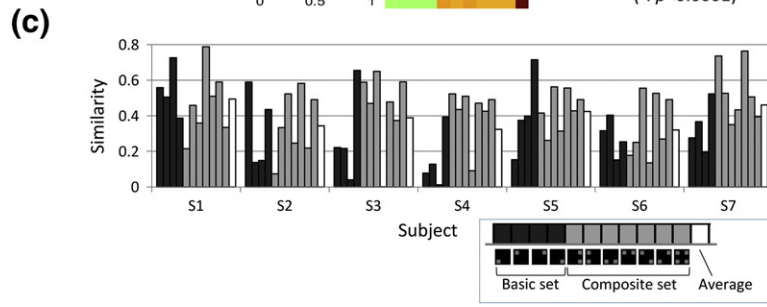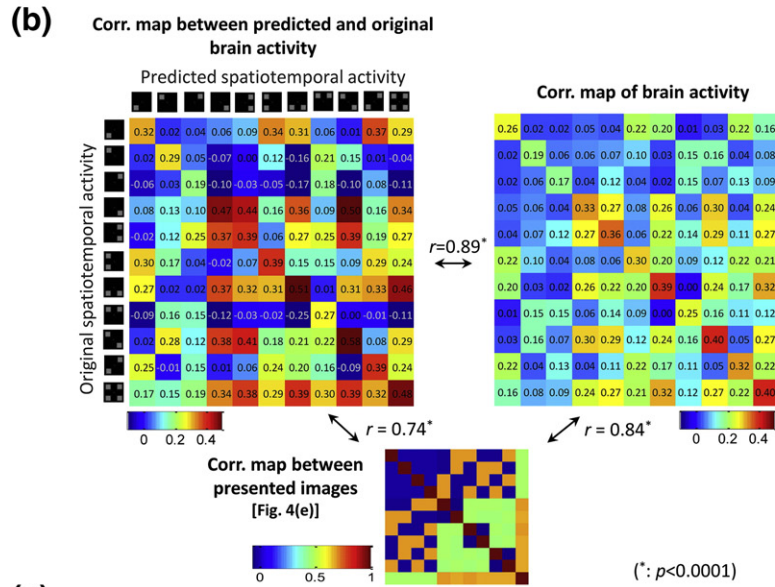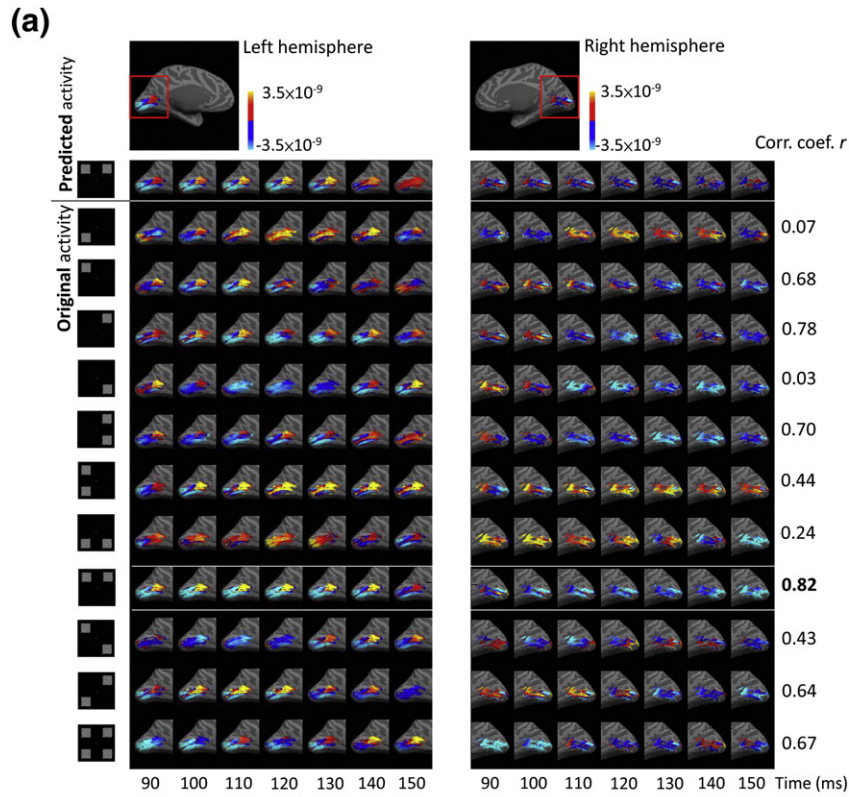
Classification

Fig. 7(a) presents the classification accuracy for all subjects using the basic set of images (black bars) and all images (white bars) containing both the basic and composite sets as visual stimuli. The brain activity in V1 with 100-ms time window from 60 ms to 160 ms was used for classification. The horizontal lines indicate the chance levels (25% for the basic image set containing four types of stimuli and 9.09% for all images containing eleven types of stimuli). Fig. 7(b) depicts the classification accuracy (averaged over seven subjects) for brain activity estimated in various Brodmann areas using the MEG measurements within 100-ms time window (60–160 ms) evoked by the basic image set. This study achieved 72.4%, 70%, and 67.3% classification accuracy for the primary (BA17), secondary (BA18), and associative visual cortices (BA19), respectively. The dashed line indicates the chance level (25%). For regions BA7, BA37, and BA39, which are related to visual processing, classification accuracy was approximately 50%. For areas apart from the visual cortices and the areas unrelated to visual processing, classification accuracy fell to approximately chance level (25%).

As shown in Fig. 7(c), the classification accuracy using brain activity in V1 evoked by four types of basic images was evaluated for a 100-ms time window moving from −150 ms to 430 ms. The dashed line indicates the chance level (25%). For all of the seven subjects, the accuracy was relatively high within the range from 70 ms to 190 ms, compared with those values obtained in other time intervals.

Fig. 7(d) presents the classification accuracy (averaged for seven subjects) evaluated for brain activity in six visual-related areas within the 100-ms sliding window. BA 17 and BA 18 had the longest duration (from 50 to 270 ms) with a high degree of classification accuracy. In contrast, BA 39 had a shorter interval (from 90 to 210 ms) with high accuracy. The classification accuracy obtained from BA 17 or BA 18 rose at an earlier stage than those obtained from other areas in the visual pathway.

Fig. 8 shows the classification results for evaluating the discriminative property of data after applying different methods on the spatial and temporal domains of brain activity. When PCA was applied in the

temporal domain, as indicated by the black bars in Fig. 8, the classification accuracy values were 72.4, 50.0, and 51.6 when LLE, spatial PCA, and none of both methods were applied in the spatial domain,

respectively. Classification accuracy was significantly higher ($p < 0.005$) when the LLE manifold was used to represent the spatial distribution of brain activity, regardless of whether the temporal PCA was applied in the temporal domain. We also compared the classification accuracy with and without the application of PCA to the temporal information. When signal powers were used instead of applying PCA, as shown by the gray bars in Fig. 8, the accuracy values were 42.6, 28.7, and 28.9 when LLE, spatial PCA, and none of both methods were applied in the spatial domain, respectively. Classification accuracy was significantly higher ($p < 0.005$) when temporal PCA was applied than using signal powers.

Manifold representation in low dimensional space

Fig. 9(a) shows a two-dimensional subspace (obtained by linear discriminant analysis) of the eight-dimensional manifold for Subject S1. Eight types of stimuli with checkerboard patches on the positions that can be categorized into purely left, right, bottom, or top are shown in this figure. This two-dimensional subspace of manifold embedded the information related to the spatial layout (left/right and bottom/top) of checkerboard patches. As shown in the left panel of Fig. 9(a), one dimension of the manifold was highly correlated with the horizontal layout of the checkerboard patches ($r = 0.70$, $p < 0.001$), whereas another dimension was highly correlated with the vertical layout ($r = 0.74$, $p < 0.001$). Other four composite stimuli are indicated on the same subspace of the manifold shown in the right panel of Fig. 9(a). One dimension was also correlated with the horizontal layout (0.62, $p < 0.001$) and another dimension was correlated with the vertical layout ($r = 0.93$, $p < 0.001$).

Fig. 9(b) illustrates the distribution of the mean STCs, each of which was the average of the STCs corresponding to the same stimulus, in a two-dimensional subspace of the manifold calculated for Subject S1. Mean STCs of the composite stimuli are depicted as colored solid circles, whereas those of basic stimuli are depicted as open circles. Take the stimulus with two checkerboard patches on the left as an example to illustrate the spatial linearity property of STCs. Its predicted STC calculated by averaging the two mean STCs of its constituent basic stimuli (linked with dashed lines), as indicated by the black solid circle, was closest to the mean STC of the composite stimulus constituted by these two basic stimuli (depicted with red solid circle). Fig. 9(c) presents the spatial linearity index for each of the seven subjects. The spatial linearity index calculated using STCs was significantly higher than that calculated using brain activity in V1 (paired *t*-test: $p < 0.001$). The spatial linearity indices for the seven subjects were positively correlated with their mean similarity values of image reconstruction presented in Fig. 4(d) ($r = 0.75$, $p < 0.05$).

Discussion

We obtained four main results from our bidirectional decoding/encoding model. First, the brain activity in our experiments can be represented by STCs lying on manifolds, whose subspace reveals spatial layout of checkerboard patches in the stimulus images. Second, STCs possess high discriminative capability, particularly for those obtained in V1 within the time interval of visual processing. Third, composite visual patterns can be reconstructed from single-trial MEG signals by

using the proposed decoding model based on the spatial linearity property of brain activity. Last, the proposed encoding model can predict the brain activity from a given stimulus image containing checkerboard patches.

Manifold for the representation of neural activity

This study investigated the manifold as a representation of neural activity. Manifold learning is capable of projecting data onto a topological space according to the distribution of the original data. Within this topological space, the data are distributed more regularly and with lower dimensionality than in the original space. Seung and Lee (2000) describe how the high-level concepts of visual perception can be organized into low-dimensional manifolds. In their statement, *N* photoreceptors form an *N*-dimensional space, and the responses of all photoreceptors for each stimulus image are represented by a point within this *N*-dimensional space. The brain may recognize the same object within images presented with different views belonging to the same manifold. To investigate manifold modeling in the human brain, this study applied LLE (Roweis and Saul, 2000) to represent the cortical activation patterns in V1. Rather than Euclidian distance, this study used spatial correlation as the distance metric between two points in the original space in order to avoid the influence of the overall magnitude of brain activity. The modified LLE method can be used to obtain a low-dimensional space embedded with the spatial layout information of checkerboard patches. High correlation coefficient was found between the spatial layout of stimulus image and the distribution of the STCs in low-dimensional space. In addition, for composite stimulus images with two checkerboard patches on the same sides, the corresponding STCs were located between the two STC distributions of the constituent basic stimulus images, as shown in the right panel of Fig. 9(a). These results suggest that the manifold-based model could be used to represent high-level visual information.

PCA is probably the most widely-used method for dimension reduction. PCA linearly transforms the data onto a subspace retaining the maximum amount of data variation. However, data variation is inherently a Euclidean distance metric and is not suitable as a similarity metric for characterizing the global structure of data distributed on a manifold. Because the spatial maps of brain activity in V1 were considered lying on a manifold, in this study LLE was chosen for dimension reduction. For comparison, we also applied PCA to extract spatial features and demonstrated that the classification accuracy was significantly lower than applying LLE, as shown in Fig. 8.

The spatial linearity or superposition of brain activity is an essential property associated with the manifold representation space. Based on the superposition principle, the brain activity evoked by a composite image can be approximated by a linear combination of the brain responses evoked by the constituent basic images. One previous fMRI study used wedges and rings as visual stimuli to demonstrate the spatial linearity of BOLD responses (Hansen et al., 2004). This study investigated the spatial linearity in VEF. We compared the predicted STC with the actual ones and the combination of basic stimuli with the composite ones. Correlation coefficient between these two comparison results was used to assess the spatial linearity property of STCs. Compared to the spatiotemporal brain activity in V1, the significantly higher spatial

Fig. 6. Results of encoding visual stimulus into brain activity. (a) The spatial distribution of the original and predicted brain activity. Each row illustrates the spatiotemporal brain activity in the left and right hemispheres at intervals between 90 ms and 150 ms after the stimulus onset. The first row presents an example of the predicted brain activity calculated by the proposed encoding process using the stimulus image with two checkerboard patches appearing on top. The following rows depict the original brain activity estimated by MCB using MEG signals evoked by eleven types of stimulus images. The rightmost column presents the spatiotemporal correlation coefficients between the predicted brain activity and the original ones. (b) Top left: correlation map between the predicted and original spatiotemporal brain activity. The correlation coefficients were calculated for each combination of the predicted and original brain activity resulting from eleven types of stimulus images. Each value of the correlation coefficient was averaged across all subjects and all trials. Top right: correlation map of original brain activity. Each value of the correlation coefficient was averaged across all subjects and all trials. Bottom: correlation map between the presented stimulus images, reduced from Fig. 4(e). These three correlation maps were all mutually correlated ($r = 0.74$, 0.84, and 0.89, $p < 0.0001$). (c) Similarity values between predicted and original spatiotemporal activity corresponding to the same stimulus image. For each subject, the similarity values are indicated by black and gray bars for basic and composite image sets, respectively, and the average similarity values across all kinds of stimulus images are indicated by white bars.
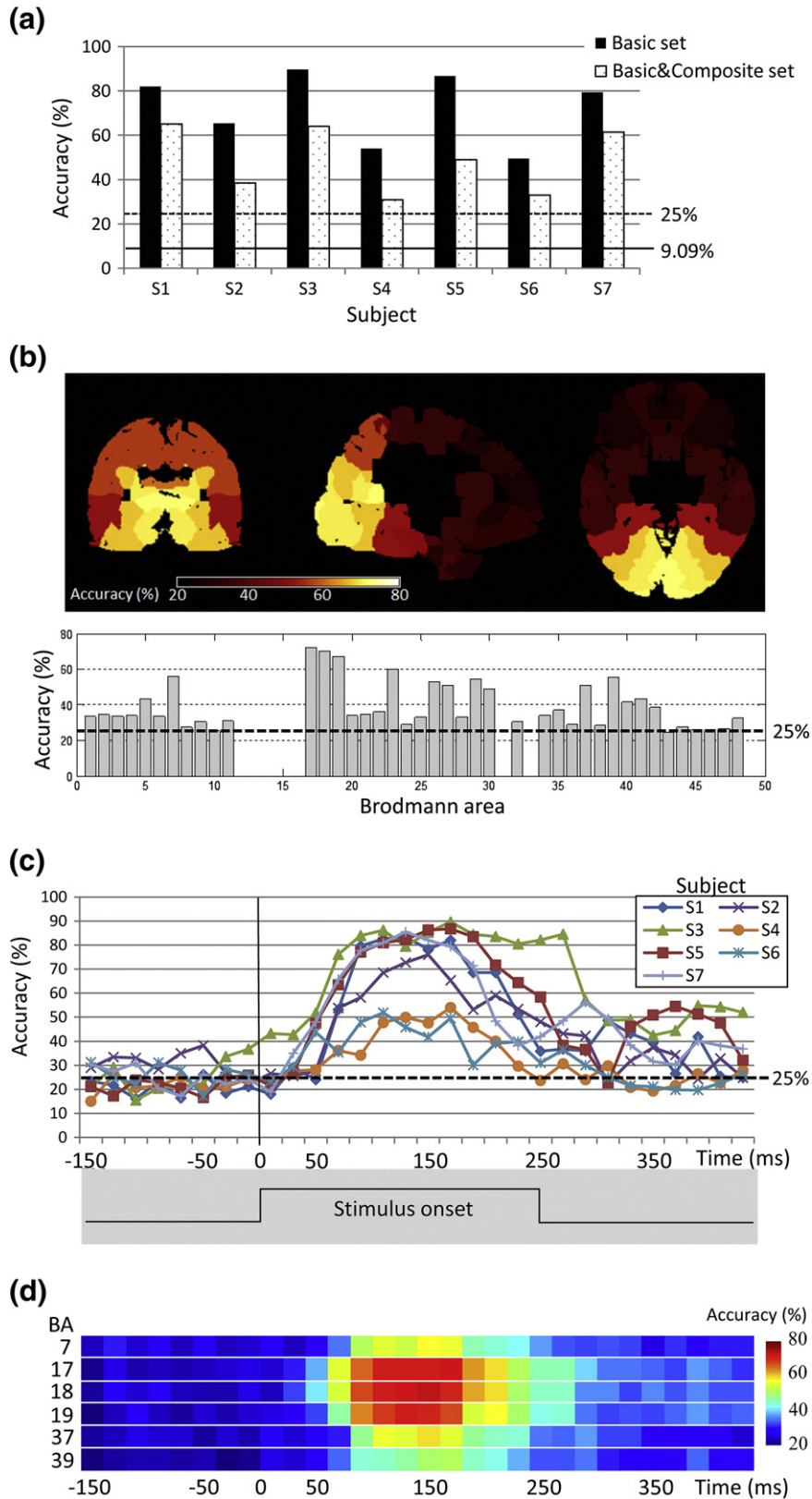
Fig. 7. Accuracy of brain activity classification using STCs. (a) Classification accuracy for each subject presented with the basic set of images (black bars) and both basic and composite sets of images (white bars). The dashed and solid lines indicate the chance levels when the stimulus image was chosen from the basic and the basic&composite image sets, respectively. (b) Classification accuracy was averaged across the seven subjects using the brain activity in each single Brodmann area. The upper panel depicts the accuracy in the sagittal, coronal, and axial views. The bottom panel presents accuracy values for all areas. Only the basic set of images was used and the dashed line indicates the chance level. (c) Classification accuracy was obtained for each subject sampled at intervals of 20 ms ranging from −150 ms to 430 ms using a 100-ms time window. The dashed line indicates the chance level. (d) For Brodmann areas 7, 17, 18, 19, 37, and 39 related to visual processing, the classification accuracy averaged across the seven subjects was higher in visual-related time intervals than those in other intervals.
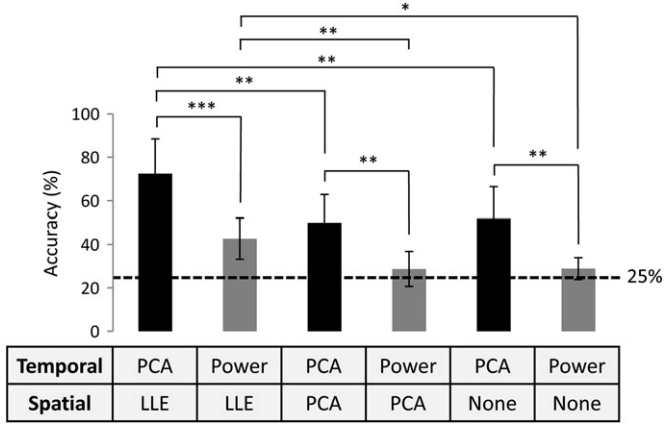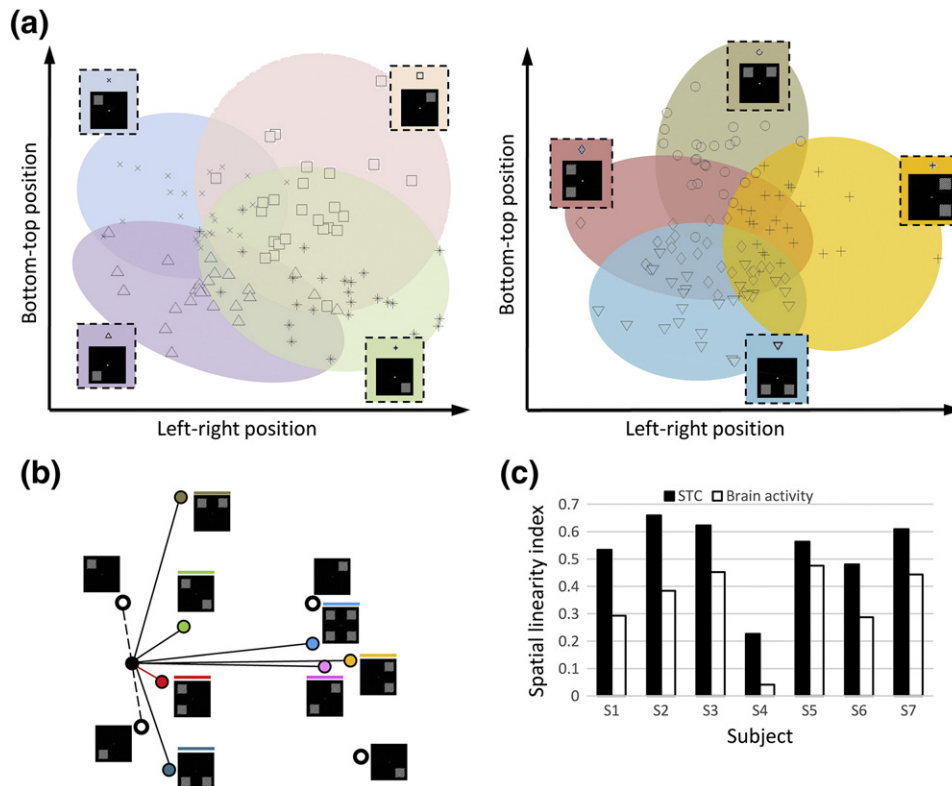
Fig. 8. Classification accuracy using different methods of extracting temporal and spatial features. Black bars depict the results with or without the use of LLE or spatial PCA for the extraction of spatial features while using PCA for temporal feature extraction. Gray bars depict the results obtained from three different spatial features using only signal powers. In both cases, the accuracy was significantly higher when LLE was used for spatial feature extraction than that when PCA or none was applied (paired *t*-test: *$p < 0.01$, **$p < 0.005$, and ***$p < 0.001$). The dashed line indicates the chance level.

indices for the seven subjects and the reconstruction similarity values suggests that the spatial linearity property of STCs could benefit the image reconstruction process.

Wavelets for the representation of image stimulus

Previous research used multi-voxel representation for the reconstruction of visual patterns from fMRI activation (Miyawaki et al., 2008). For voxel-based representation, Kamitani and Tong (2005) synthesized fMRI responses in V1 by applying Gabor-like filters to visual stimuli and successfully decoded the orientation information from these synthesized responses. Kay et al. (2008) used Gabor wavelets to construct a model for image identification. Naselaris et al. (2009) adopted sparse Gabor prior for the reconstruction of the natural images. Pasley et al. (2012) applied space-time Gabor filters to video sequences in an encoding model. Based on the reconstruction performance in our experiments as shown in Fig. 5, this study selected Haar wavelets to represent image stimuli, rather than Gabor wavelets. On the average for all eleven types of stimuli, the similarity values for Haar and Gabor wavelets were 0.71 and 0.32, respectively. One reason for this discrepancy may be that the visual stimuli used in this work comprised simple checkerboard patches, which can be sufficiently represented by Haar wavelets. Another reason for this choice is the fact that a large number of Gabor wavelets could increase the difficulty of estimation and negatively affect the accuracy of linear mapping between the wavelet and STC spaces. On the other hand, the insufficient number of the Gabor wavelets cannot completely represent the image (Lee, 1996) and may degrade the reconstruction performance. We suggest that the type of wavelets be chosen according to image content. Gabor wavelets may outperform Haar wavelets when dealing with complex

linearity index calculated for STCs implies the feasibility for the proposed manifold representation to reconstruct a novel composite image from a set of basic images after finding the linear combination relationship among the associated STCs. The positive correlation ($r = 0.75$, $p < 0.05$) between the spatial linearity

Fig. 9. (a) A two-dimensional subspace of the LLE manifold space. Each point indicates an STC calculated from MEG signals of Subject S1. The STCs evoked by four basic stimulus images are presented in the left panel, whereas those evoked by four composite stimulus images are presented in the right panel. Both panels show the same subspace of manifold and the distribution of STCs manifests the layout of checkerboard patches in the stimulus images. (b) Spatial distribution of mean STCs in the same two-dimensional subspace as in (a). Each mean STC was the average of all STC points for each type of stimulus image. The open circles depict the mean STCs of basic stimulus images and colored solid circles depict the mean STCs for composite stimulus images. The black solid circle depicts an example of the linear combination of two mean STCs linked by dashed lines. Solid lines show the distances between the predicted STC and the mean STCs of all composite stimuli in this two-dimensional subspace. (c) Spatial linearity index calculated using STC was significantly larger than that calculated using brain activity in V1 (paired *t*-test: $p < 0.001$).

images or those involving natural stimulus images. Another alternative is to automatically determine an image basis from the stimulus images per se. Instead of a fixed image representation, for example, Fujiwara et al. (2013) used Bayesian canonical correlation analysis (BCCA) to calculate image bases mapping from latent variables to image pixels.

Decoding the spatiotemporal information from MEG

Most previous studies have used fMRI to decode visual information (Brouwer and Heeger, 2009; Haynes and Rees, 2005; Kamitani and Tong, 2005; Kay et al., 2008; Miyawaki et al., 2008; Naselaris et al., 2009; Nishimoto et al., 2011; Schoenmakers et al., 2013; Thirion et al., 2006). Rather than the metabolic correlates of fMRI data, this study utilized neural activity measurements of MEG to enable an accurate reconstruction of visual patterns in a trial-by-trial manner.

Previous studies have demonstrated that brain source localization in V1 can be precise to 2 mm using MEG (Poghosyan and Ioannides, 2007) and the distances between peak locations identified by fMRI and MEG can be in the range of 3 to 5 mm (Moradi et al., 2003). This study calculated visual cortical activity from MEG measurements using the MCB method (Chen et al., 2006). Adaptive MCB spatial filters were derived from the MEG measurements of a particular stimulus in a data-driven manner. However, a universal spatial filter was required to cope with unknown situations in the decoding process. One approach to designing this kind of universal spatial filter involves maximizing the inter-stimulus variance while minimizing intra-stimulus variance (Muller-Gerking et al., 1999; Xiang et al., 2007). This design emphasizes the differences between stimuli while disregarding common properties among stimuli, making it unsuitable for image reconstruction. This study calculated the universal spatial filter by averaging the spatial filters obtained from four basic image stimuli. Spatial filters designed in this manner are capable of preserving both common and event-specific characteristics in the estimated brain activity.

The early response (N70m) between 50 ms and 100 ms following stimulus onset (Carandini et al., 2005; Inui and Kakigi, 2006; Laskaris et al., 2003; Tzelepi et al., 2001; Vanni et al., 2001) plays an important role in the classification of visual patterns because classification accuracy is far higher during the VEF period than during other intervals, as shown in Fig. 7(c). The durations for above-chance decoding are consistent with previous findings related to visual processing in which V1 neurons are attuned to patterns with spatial differences in early stages (40 ms or further) (Tong, 2003). The similar time-resolved decoding results were also found in the previous study (Ramkumar et al., 2013). These results suggest that the temporal resolution of MEG can help to reveal the rapid visual perception process. It should be noted that, in this study, the offset of the visual stimulus at 250 ms after the onset also evoked a VEF at approximately 350 ms (Parker et al., 1982), which tends to slightly enhance classification accuracy.

As shown in Fig. 7(b), classification accuracy was higher when involving the regions along the dorsal and ventral visual pathways than when using estimated brain activity in other regions. Fig. 7(d) shows the time delay involved in classification accuracy in regions related to visual processing. In the associative visual cortex (BA 19), classification accuracy increased at a point approximately 20 ms later than in V1 (Bullier, 2001). Moreover, the intervals with high classification accuracy were longer in V1 and V2 than in other visual cortices. These results support the integrated (interactive) model proposed in previous studies: V1 has interactive connections with many extrastriate areas (V2, V3, V3A, V4 and MT), and receives feedback signals during conscious perception (Bullier, 2001; Lamme and Roelfsema, 2000; Tong, 2003).

From the brain activity estimated using MCB spatial filters, this study extracted VEF components using temporal PCA. This procedure was used to extract the event-related potential components mentioned in previous EEG studies (Dien, 2012; Dien et al., 2005). To investigate the importance of temporal information, we classified brain activity based on the temporal and spatial information obtained using different

methods shown in Fig. 8. Regardless of whether LLE or spatial PCA was used for extracting spatial features, the accuracy was higher when the TPCs calculated with temporal PCA were used for classification (black bars), compared to that when the powers of the estimated brain activity were used (gray bars). This indicates that temporal information in brain activity is helpful for the differentiation of brain responses corresponding to different experimental conditions.

From the reconstruction results of the seven subjects shown in Fig. 4(d), we found that the mean similarity between the original and reconstructed stimulus images with checkerboard patches in lower visual field was 0.80, which was significantly higher than the similarity value 0.73 observed with patches in the upper visual field (Fisher's transformation $z = 7.78$, $p < 0.001$). However, there was no significant difference between the mean similarity values for the left (0.71) and right (0.69) visual fields (Fisher's transformation $z = 1.80$, $p = 0.07$). One possible explanation of this phenomenon is that visual performance in the lower visual field is better than that in the upper visual field, according to the visual field asymmetry (Berardi and Fiorentini, 1991; Levine and McAnany, 2005; Portin et al., 1998).

Encoding the visual stimulus image

Accurate encoding model can facilitate the investigation of computational theories of perception and cognition (Serences and Saproo, 2012). The proposed encoding model can accurately predict the neural activity in V1 for stimulus images containing checkerboard patches, as shown by the high similarity values of diagonal elements in the correlation map between the predicted and original brain activity. Moreover, the whole predicted/original brain activity correlation map is highly correlated to the original brain activity correlation map ($r = 0.89$, $p < 0.0001$), as shown in Fig. 6(b). That is, similar predicted brain signals for two different image stimuli implied that similar brain signals were observed for these two image stimuli.

As shown in Fig. 6(b), some non-diagonal elements in the three correlation maps have large values. In the stimulus image correlation map, the values on non-diagonal elements are large when checkerboard patches exist in some common quadrants of the corresponding two stimulus images. In the original brain activity correlation map, non-diagonal elements with large values indicate that the corresponding brain signals were evoked by stimulus images with common checkerboard patches. The highly positive correlation coefficient ($r = 0.84$, $p < 0.0001$) between image stimulus correlation map and original brain activity correlation map can be attributed to spatial linearity of retinotopic responses (Hansen et al., 2004). That is, brain activity evoked by a composite stimulus image is similar to those evoked by its composing basic stimulus images.

More importantly, in the predicted/original brain activity correlation map, the correlation coefficients are relatively large when there are common checkerboard patches in some quadrants of the corresponding stimulus images. For example, the correlation value of element (4, 9), 0.50, is close to that of the diagonal element (9, 9), 0.58, because the stimulus images corresponding to these two elements both have the checkerboard patch at the right-bottom quadrant. Conversely, the correlation coefficient is relatively small when the checkerboard patches are at different locations. For example, the correlation value of element (10, 9) is −0.09. The significant positive correlation coefficient value between the predicted/original brain activity correlation map and stimulus image correlation map ($r = 0.74$, $p < 0.0001$) indicates that the specificity of the predicted brain signals is caused by the dissimilarity of the stimulus images.

Previous fMRI studies used encoding models to predict the BOLD response patterns evoked by visual stimuli (Kay et al., 2008; Mitchell et al., 2008). The 1-Hz BOLD signals with temporal information were predicted in a previous study (Nishimoto et al., 2011). Sprague and Serences (2013) used fMRI and encoding model to reconstruct spatial representation of visual stimuli. Fujiwara et al. (2013) also developed the BCCA

method to derive a bidirectional model for visual stimuli. In addition to the decoding of fMRI activity, they also demonstrated the results of encoding visual stimulus by using latent variables, image bases, and voxel weights. The main difference between this study and previous ones is that the proposed encoding model can be used to predict spatio-temporal neural activity. In other words, it is possible to predict temporal signals at the millisecond level for each position in the brain. Although elementary checkerboard patches were used to constitute test images, to the best of our knowledge, this is the first attempt to investigate the prediction of neural activity with high spatial as well as temporal resolutions. The ability to reveal temporal changes in brain activity from the encoding model is crucial to uncovering the means by which visual processes are organized to produce visual perception.

Conclusions

Our results using MEG have demonstrated the efficacy of the proposed bidirectional model in both decoding brain activity and encoding visual stimuli using checkerboard image patches. Two-dimensional wavelets can capture important image features to compactly represent the stimulus images containing checkerboard patches. By mapping the high-dimensional data of neural activity to a low-dimensional space, manifold representation can effectively model the spatiotemporal dynamics of neural activity associated with visual processing. The decoding model based on this manifold representation is generalizable, such that a model trained using basic images can be used to reconstruct composite stimulus images. The reconstruction results from single-trial MEG data also suggest the possibility of real-time image reconstruction. Furthermore, the spatiotemporal brain activity for a given stimulus image containing checkerboard patches can be accurately predicted using the encoding process of the proposed model.

Acknowledgments

Conflict of interest

The authors declare that there are no conflicts of interest.

References

Ahlfors, S.P., Simpson, G.V., Dale, A.M., Belliveau, J.W., Liu, A.K., Korvenoja, A., Virtanen, J., Huotilainen, M., Tootell, R.B., Aronen, H.J., Ilmoniemi, R.J., 1999. Spatiotemporal activity of a cortical network for processing visual motion revealed by MEG and fMRI. J. Neurophysiol. 82, 2545.

Ayzenshtat, I., Meirovithz, E., Edelman, H., Werner-Reiss, U., Bienenstock, E., Abeles, M., Slovin, H., 2010. Precise spatiotemporal patterns among visual cortical areas and their relation to visual stimulus processing. J. Neurosci. 30, 11232–11245.

Berardi, N., Fiorentini, A., 1991. Visual field asymmetries in pattern discrimination: a sign of asymmetry in cortical visual field representation? Vis. Res. 31, 1831–1836.

Bradberry, T.J., Gentili, R.J., Contreras-Vidal, J.L., 2010. Reconstructing three-dimensional hand movements from noninvasive electroencephalographic signals. J. Neurosci. 30, 3432–3437.

Brewer, A.A., Liu, J., Wade, A.R., Wandell, B.A., 2005. Visual field maps and stimulus selectivity in human ventral occipital cortex. Nat. Neurosci. 8, 1102–1109.

Brouwer, G.J., Heeger, D.J., 2009. Decoding and reconstructing color from responses in human visual cortex. J. Neurosci. 29, 13992–14003.

Bullier, J., 2001. Integrated model of visual processing. Brain Res. Brain Res. Rev. 36, 96–107.

Carandini, M., Demb, J.B., Mante, V., Tolhurst, D.J., Dan, Y., Olshausen, B.A., Gallant, J.L., Rust, N.C., 2005. Do we know what the early visual system does? J. Neurosci. 25, 10577–10597.

Chang, C.C., Lin, C.J., 2011. LIBSVM: a library for support vector machines. ACM Trans. Intell. Syst. Technol. 2, 1–27.

Chen, Y.S., Cheng, C.Y., Hsieh, J.C., Chen, L.F., 2006. Maximum contrast beamformer for electromagnetic mapping of brain activity. IEEE Trans. Biomed. Eng. 53, 1765–1774.

Cox, D.D., Savoy, R.L., 2003. Functional magnetic resonance imaging (fMRI) "brain reading": detecting and classifying distributed patterns of fMRI activity in human visual cortex. NeuroImage 19, 261–270.

De Martino, F., Valente, G., Staeren, N., Ashburner, J., Goebel, R., Formisano, E., 2008. Combining multivariate voxel selection and support vector machines for mapping and classification of fMRI spatial patterns. NeuroImage 43, 44–58.

Dien, J., 2012. Applying principal components analysis to event-related potentials: a tutorial. Dev. Neuropsychol. 37, 497–517.

Dien, J., Beal, D.J., Berg, P., 2005. Optimizing principal components analysis of event-related potentials: matrix type, factor loading weighting, extraction, and rotations. Clin. Neurophysiol. 116, 1808–1825.

Duncan, K.K., Hadjipapas, A., Li, S., Kourtzi, Z., Bagshaw, A., Barnes, G., 2010. Identifying spatially overlapping local cortical networks with MEG. Hum. Brain Mapp. 31, 1003–1016.

Engel, S.A., Glover, G.H., Wandell, B.A., 1997. Retinotopic organization in human visual cortex and the spatial precision of functional MRI. Cereb. Cortex 7, 181–192.

Formisano, E., De Martino, F., Bonte, M., Goebel, R., 2008. "Who" is saying "what"? Brain-based decoding of human voice and speech. Science 322, 970–973.

Fujiwara, Y., Miyawaki, Y., Kamitani, Y., 2013. Modular encoding and decoding models derived from Bayesian canonical correlation analysis. Neural Comput. 25, 979–1005.

Gallivan, J.P., McLean, D.A., Valyear, K.F., Pettypiece, C.E., Culham, J.C., 2011. Decoding action intentions from preparatory brain activity in human parieto-frontal networks. J. Neurosci. 31, 9599–9610.

Hansen, K.A., David, S.V., Gallant, J.L., 2004. Parametric reverse correlation reveals spatial linearity of retinotopic human V1 BOLD response. NeuroImage 23, 233–241.

Haxby, J.V., Gobbini, M.I., Furey, M.L., Ishai, A., Schouten, J.L., Pietrini, P., 2001. Distributed and overlapping representations of faces and objects in ventral temporal cortex. Science 293, 2425–2430.

Haynes, J.D., Rees, G., 2005. Predicting the orientation of invisible stimuli from activity in human primary visual cortex. Nat. Neurosci. 8, 591–686.

Haynes, J.D., Rees, G., 2006. Decoding mental states from brain activity in humans. Nat. Rev. Neurosci. 7, 523–534.

Inui, K., Kakigi, R., 2006. Temporal analysis of the flow from V1 to the extrastriate cortex in humans. J. Neurophysiol. 96, 775–784.

Ioannides, A.A., Poghosyan, V., Liu, L., Saridis, G.A., Tamietto, M., Op de Beeck, M., De Tiege, X., Weiskrantz, L., de Gelder, B., 2012. Spatiotemporal profiles of visual processing with and without primary visual cortex. NeuroImage 63, 1464–1477.

Jones, J.P., Palmer, L.A., 1987. An evaluation of the two-dimensional Gabor filter model of simple receptive fields in cat striate cortex. J. Neurophysiol. 58, 1233–1258.

Kamitani, Y., Tong, F., 2005. Decoding the visual and subjective contents of the human brain. Nat. Neurosci. 8, 679–685.

Kay, K.N., Naselaris, T., Prenger, R.J., Gallant, J.L., 2008. Identifying natural images from human brain activity. Nature 452, 352–355.

Koskinen, M., Viinikanoja, J., Kurimo, M., Klami, A., Kaski, S., Hari, R., 2013. Identifying fragments of natural speech from the listener's MEG signals. Hum. Brain Mapp. 34, 1477–1489.

Kriegeskorte, N., 2011. Pattern-information analysis: from stimulus decoding to computational-model testing. NeuroImage 56, 411–421.

LaConte, S.M., Peltier, S.J., Hu, X.P., 2007. Real-time fMRI using brain-state classification. Hum. Brain Mapp. 28, 1033–1044.

Lamme, V.A., Roelfsema, P.R., 2000. The distinct modes of vision offered by feedforward and recurrent processing. Trends Neurosci. 23, 571–579.

Laskaris, N.A., Liu, L.C., Ioannides, A.A., 2003. Single-trial variability in early visual neuromagnetic responses: an explorative study based on the regional activation contributing to the N70m peak. NeuroImage 20, 765–783.

Lee, T.S., 1996. Image representation using 2D Gabor wavelets. IEEE Trans. Pattern Anal. Mach. Intell. 18, 959–971.

Levine, M.W., McAnany, J.J., 2005. The relative capabilities of the upper and lower visual hemifields. Vis. Res. 45, 2820–2830.

Liang, M., Mouraux, A., Hu, L., Iannetti, G.D., 2013. Primary sensory cortices contain distinguishable spatial patterns of activity for each sense. Nat. Commun. 4, 1979.

Miikkulainen, R., Bednar, J.A., Choe, Y., Sirosh, J., 2005. Computational Maps in the Visual Cortex. Springer Science+Business Media, Inc., New York, NY.

Mitchell, T.M., Shinkareva, S.V., Carlson, A., Chang, K.M., Malave, V.L., Mason, R.A., Just, M.A., 2008. Predicting human brain activity associated with the meanings of nouns. Science 320, 1191–1195.

Miyawaki, Y., Uchida, H., Yamashita, O., Sato, M.A., Morito, Y., Tanabe, H.C., Sadato, N., Kamitani, Y., 2008. Visual image reconstruction from human brain activity using a combination of multiscale local image decoders. Neuron 60, 915–929.

Moradi, F., Liu, L.C., Cheng, K., Waggoner, R.A., Tanaka, K., Ioannides, A.A., 2003. Consistent and precise localization of brain activity in human primary visual cortex by MEG and fMRI. NeuroImage 18, 595–609.

Muller-Gerking, J., Pfurtscheller, G., Flyvbjerg, H., 1999. Designing optimal spatial filters for single-trial EEG classification in a movement task. Clin. Neurophysiol. 110, 787–798.

Naselaris, T., Prenger, R.J., Kay, K.N., Oliver, M., Gallant, J.L., 2009. Bayesian reconstruction of natural images from human brain activity. Neuron 63, 902–915.

Naselaris, T., Kay, K.N., Nishimoto, S., Gallant, J.L., 2011. Encoding and decoding in fMRI. NeuroImage 56, 400–410.

Nishimoto, S., Vu, A.T., Naselaris, T., Benjamini, Y., Yu, B., Gallant, J.L., 2011. Reconstructing visual experiences from brain activity evoked by natural movies. Curr. Biol. 21, 1641–1646.

Norman, K.A., Polyn, S.M., Detre, G.J., Haxby, J.V., 2006. Beyond mind-reading: multi-voxel pattern analysis of fMRI data. Trends Cogn. Sci. 10, 424–430.

Ogmen, H., Herzog, M.H., 2010. The geometry of visual perception: retinotopic and non-retinotopic representations in the human visual system. Proc. IEEE Inst. Electr. Eng. 98, 479–492.

Parker, D.M., Salzen, E.A., Lishman, J.R., 1982. Visual-evoked responses elicited by the onset and offset of sinusoidal gratings: latency, waveform, and topographic characteristics. Invest. Ophthalmol. Vis. Sci. 22, 675–680.

Parkes, L.M., Marsman, J.B., Oxley, D.C., Goulermas, J.Y., Wuerger, S.M., 2009. Multivoxel fMRI analysis of color tuning in human primary visual cortex. J. Vis. 9, 1–13.

Pasley, B.N., David, S.V., Mesgarani, N., Flinker, A., Shamma, S.A., Crone, N.E., Knight, R.T., Chang, E.F., 2012. Reconstructing speech from human auditory cortex. PLoS Biol. 10, e1001251.

Poghosyan, V., Ioannides, A.A., 2007. Precise mapping of early visual responses in space and time. NeuroImage 35, 759–770.

Portin, K., Salenius, S., Salmelin, R., Hari, R., 1998. Activation of the human occipital and parietal cortex by pattern and luminance stimuli: neuromagnetic measurements. Cereb. Cortex 8, 253–260.

Ramkumar, P., Jas, M., Pannasch, S., Hari, R., Parkkonen, L., 2013. Feature-specific information processing precedes concerted activation in human visual cortex. J. Neurosci. 33, 7691–7699.

Reddy, L., Tsuchiya, N., Serre, T., 2010. Reading the mind's eye: decoding category information during mental imagery. NeuroImage 50, 818–825.

Ritter, H., Martinetz, T., Schulten, K., 1992. Neural Computation and Self-organizing Maps: An Introduction. Addison Wesley Longman Publishing Co., Inc.

Roweis, S.T., Saul, L.K., 2000. Nonlinear dimensionality reduction by locally linear embedding. Science 290, 2323–2326.

Schoenmakers, S., Barth, M., Heskes, T., van Gerven, M., 2013. Linear reconstruction of perceived images from human brain activity. NeuroImage 83, 951–961.

Serences, J.T., Saproo, S., 2012. Computational advances towards linking BOLD and behavior. Neuropsychologia 50, 435–446.

Sereno, M.I., Dale, A.M., Reppas, J.B., Kwong, K.K., Belliveau, J.W., Brady, T.J., Rosen, B.R., Tootell, R.B., 1995. Borders of multiple visual areas in humans revealed by functional magnetic resonance imaging. Science 268, 889–893.

Seung, H.S., Lee, D.D., 2000. Cognition. The manifold ways of perception. Science 290, 2268–2269.

Sprague, T.C., Serences, J.T., 2013. Attention modulates spatial priority maps in the human occipital, parietal and frontal cortices. Nat. Neurosci. 16, 1879–1887.

Tenenbaum, J.B., de Silva, V., Langford, J.C., 2000. A global geometric framework for nonlinear dimensionality reduction. Science 290, 2319–2323.

Thirion, B., Duchesnay, E., Hubbard, E., Dubois, J., Poline, J.B., Lebihan, D., Dehaene, S., 2006. Inverse retinotopy: inferring the visual content of images from brain activation patterns. NeuroImage 33, 1104–1116.

Tong, F., 2003. Primary visual cortex and visual awareness. Nat. Rev. Neurosci. 4, 219–229.

Tzelepi, A., Ioannides, A.A., Poghosyan, V., 2001. Early (N70m) neuromagnetic signal topography and striate and extrastriate generators following pattern onset quadrant stimulation. NeuroImage 13, 702–718.

Uusitalo, M.A., Ilmoniemi, R.J., 1997. Signal-space projection method for separating MEG or EEG into components. Med. Biol. Eng. Comput. 35, 135–140.

van de Nieuwenhuijzen, M.E., Backus, A.R., Bahramisharif, A., Doeller, C.F., Jensen, O., van Gerven, M.A., 2013. MEG-based decoding of the spatiotemporal dynamics of visual category perception. NeuroImage 83, 1063–1073.

Vanni, S., Tanskanen, T., Seppa, M., Uutela, K., Hari, R., 2001. Coinciding early activation of the human primary visual cortex and anteromedial cuneus. Proc. Natl. Acad. Sci. U. S. A. 98, 2776–2780.

Wandell, B.A., Dumoulin, S.O., Brewer, A.A., 2007. Visual field maps in human cortex. Neuron 56, 366–383.

Xiang, L., Dezhong, Y., Dan, W., Chaoyi, L., 2007. Combining spatial filters for the classification of single-trial EEG in a finger movement task. IEEE Trans. Biomed. Eng. 54, 821–831.